The Astrophysical Journal, 997:189 (16pp), 2026 February 1 https://doi.org/10.3847/1538-4357/ae247c

Feeding the Dead: Neutral Gas Inflow in a Long-quenched Ancient Massive Galaxy at $z \sim 2.7$ Observed with JWST/NIRSpec

Davide Bevacqua[1,2], Danilo Marchesini[1], Paolo Saracco[2], Francesco La Barbera[3], Richard Pan[1], Sirio Belli[4], Gabriel Brammer[5], Guido De Marchi[6], Fabio R. Ditrani[7,8], Giovanna Giardino[9], Karl Glazebrook[10], Valentina La Torre[1], Jamie Lin[1], Adam Muzzin[11], Namrata Roy[12,13], Paola Santini[14], Benedetta Vulcani[15], Peter J. Watson[15], and Xin Wang[16,17,18]

[1] Physics and Astronomy Department, Tufts University, 574 Boston Avenue, Medford, MA 02155, USA; davide.bevacqua@inaf.it
[2] INAF—Osservatorio Astronomico di Brera, via Brera 28, 20121 Milano, Italy
[3] INAF—Osservatorio Astronomico di Capodimonte, Via Moiariello 16, 80131, Naples, Italy
[4] Dipartimento di Fisica e Astronomia, Universitá di Bologna, Via Gobetti 93/2, I-40129, Bologna, Italy
[5] Niels Bohr Institute, University of Copenhagen, Jagtvej 128, Copenhagen, Denmark
[6] European Space Research and Technology Centre, Keplerlaan 1, 2200 AG Noordwijk, The Netherlands
[7] Universitá degli studi di Milano-Bicocca, Piazza della scienza, I-20125 Milano, Italy
[8] INAF—Osservatorio Astronomico di Brera, via Brera 28, I-20121 Milano, Italy
[9] ATG Europe for the European Space Agency, European Space Research and Technology Centre, Noordwijk, The Netherlands
[10] Centre for Astrophysics and Supercomputing, Swinburne University of Technology, PO Box 218, Hawthorn, VIC 3122, Australia
[11] Department of Physics and Astronomy, York University, 4700 Keele Street, Toronto, ON M3J 1P3, Canada
[12] School of Earth and Space Exploration, Arizona State University, Tempe, AZ 85281, USA
[13] Department of Physics & Astronomy, Johns Hopkins University, Baltimore, MD 21218, USA
[14] INAF—Osservatorio Astronomico di Roma, via di Frascati 33, 00078, Monte Porzio Catone, Roma, Italy
[15] INAF—Osservatorio astronomico di Padova, Vicolo Osservatorio 5, I-35122 Padova, Italy
[16] School of Astronomy and Space Science, University of Chinese Academy of Sciences (UCAS), Beijing 100049, People's Republic of China
[17] National Astronomical Observatories, Chinese Academy of Sciences, Beijing 100101, People's Republic of China
[18] Institute for Frontiers in Astronomy and Astrophysics, Beijing Normal University, Beijing 102206, People's Republic of China
Received 2025 October 13; revised 2025 November 24; accepted 2025 November 24; published 2026 January 22

Abstract

We report the spectroscopic detection of neutral gas inflow into a massive ($M_* \simeq 4 \times 10^{10}\,M_\odot$) quiescent galaxy observed at $z_{\rm spec} = 2.6576$ with the James Webb Space Telescope (JWST). From the redshifted absorption of the Na I doublet at $\lambda\lambda$5890, 5896, we estimate an inflow velocity $v = 278^{+79}_{-79}$ km s^{-1} and a column density $\log(N_{\rm NaI}/{\rm cm}^2) = 13.02^{+0.03}_{-0.03}$. We derive the inflowing mass of the gas $M_{\rm in} = 1.6^{+0.1}_{-0.1} \times 10^8\,M_\odot$ and rate $\dot{M}_{\rm in} = 19^{+6}_{-7}\,M_\odot\,{\rm yr}^{-1}$. The presence of several surrounding galaxies suggests that the galaxy may be accreting gas from nearby companions. However, we cannot confirm this with current data, and the intergalactic medium or cosmic filaments are also viable sources of the inflowing gas. Despite the ongoing inflow, the galaxy remains quiescent, with an upper limit to the star formation rate of $0.2\,M_\odot\,{\rm yr}^{-1}$. Moreover, its star formation history suggests that the galaxy has remained quiescent during the past $\sim$1 Gyr, with half of its stars formed by redshift $z_{50} = 11^{+18}_{-3}$. We discuss that the inflow is not massive, dense, or long-lived enough to ignite significant star formation (SF), or it is fueling low-level active galactic nucleus activity instead. This is direct evidence that quiescent galaxies can accrete cold gas after their quenching while keeping their SF subdued. Follow-up observations with JWST and the Atacama Large Millimeter/submillimeter Array will be needed to constraint the nature of the inflowing gas.

Unified Astronomy Thesaurus concepts: Galaxies (573); High-redshift galaxies (734); Post-starburst galaxies (2176); Galaxy spectroscopy (2171); Cold neutral medium (266); Galaxy quenching (2040); Quenched galaxies (2016); Star formation (1569)

1. Introduction

In the standard paradigm of galaxy formation, galaxies grow through the accretion of gas from the cosmic web, which fuels star formation (SF) and the growth of central supermassive black holes (e.g., S. D. M. White & M. J. Rees 1978; A. Dekel et al. 2009). Over cosmic time, galaxies can run out of cold gas, stop their SF (or "quench"), and become quiescent. Despite the cessation of SF, quiescent galaxies can continue to interact with their surroundings, accreting gas from the cosmic web or close companions, eventually igniting new SF or active galactic nucleus (AGN) activity.

Many observational studies (e.g., P. Chauke et al. 2019; C. Mancini et al. 2019; S. Tacchella et al. 2022; C. Woodrum et al. 2022; T. S. Tanaka et al. 2024) and simulations (e.g., R. Davé et al. 2020; M. P. Rey et al. 2020; R.-S. Remus & L. C. Kimmig 2025) indicate that quiescent galaxies can undergo major episodes of SF after their quenching, causing rejuvenation. The detection of nonnegligible fractions of cold gas in a large number of quiescent galaxies at both low and high z (M. T. Sargent et al. 2015; J. Spilker et al. 2018; R. Gobat et al. 2020; C. Woodrum et al. 2022; J. C. Siegel et al. 2025) suggests that they can continue to accrete gas after their quenching, replenishing their gas content while still being classified as quiescent according to standard diagnostics (e.g.,

S. Belli et al. 2017, 2021; R. Gobat et al. 2020; N. Salvador-Rusiñol et al. 2020) that might fuel future rejuvenation. However, the origin and fate of cold gas in quiescent galaxies remains an open issue.

In general, galaxies can accrete gas from a variety of sources, such as the cosmic web, close companions, or the intergalactic medium (IGM), potentially reigniting SF or fuel AGN activity. Direct evidence of gas accretion is rare, and is found in galaxies across different redshifts and environments (see A. Fox & R. Davé 2017 and references therein). In the literature, gas inflows have been detected mainly in star-forming galaxies and are usually associated with ongoing SF (G. G. Kacprzak et al. 2012; K. H. R. Rubin et al. 2012, 2022; S. H. Ho et al. 2017; A. Weldon et al. 2023; E. Coleman et al. 2024). In contrast, the detection of neutral gas inflows in passive galaxies has been associated with AGN activity (J. H. van Gorkom et al. 1989; T. Sato et al. 2009; H. B. Krug et al. 2010; N. Roy et al. 2021; D. S. N. Rupke et al. 2021). Whether an inflow can trigger SF depends on the mode of accretion and the local physical conditions of the gas (A. Zolotov et al. 2015; S. Tacchella et al. 2016, 2020), which also depend on the source of the gas. Observations seem to indicate that there is no univocal origin for the inflowing material, and that the cosmic web, IGM, close galaxies, and recycled material from previous SF are all possible candidates (M. E. Putman 2017). Studying inflows in galaxies is fundamental to understand how gas accretion occurs, as it regulates the SF and the chemical enrichment of both the stellar and gaseous components, and thus the star formation history (SFH), as well as the activity of the central AGN. In particular, finding inflows in quiescent galaxies is uncommon, and studying such rare systems is essential for constraining models of galaxy quenching, as they challenge the simple picture in which the cessation of SF is accompanied by a complete shutdown of gas accretion.

In this work, we report the spectroscopic detection of neutral gas inflow into a long-quenched massive galaxy at $z_{\rm spec} = 2.6576 \pm 0.0003$ observed with the James Webb Space Telescope (JWST). Remarkably, this galaxy shows neither ongoing SF nor strong evidence for AGN activity, making it a unique study case for the coexistence of gas accretion and quenching. Interestingly, this galaxy resides in an overdensity, providing an opportunity to investigate how the environment influences the gas cycle in quiescent galaxies at early cosmic times. The JWST data allow us to characterize the stellar population properties of the galaxy and the properties of the inflowing material, and to investigate its origin. In Section 2, we present the data. In Section 3, we describe the methods we used for the analysis. We present our results in Section 4, and discuss them in Section 5. Finally, in Section 6, we present our conclusions. Throughout this paper, we assume a G. Chabrier (2003) initial mass function (IMF) and adopt a flat Lambda cold dark matter (ΛCDM) cosmology with $H_0 = 70$ km s^{-1} and $\Omega_{\rm m} = 0.3$.

2. Data

We selected our target galaxy from the GLASS-JWST Early Release Science program (T. Treu et al. 2022; D. Paris et al. 2023). The galaxy, with GLASS ID 180009 (R.A. 3.605219, decl. −30.39540; hereafter GLASS-180009), was identified as quiescent by D. Marchesini et al. (2023). This galaxy was initially selected from the HFF-DeepSpace catalogs in the Abell2744 cluster pointing constructed by H. V. Shipley et al. (2018), having a photometric redshift >2, magnitude $m_{\rm F160W} < 26$, stellar mass $>10^8\,M_\odot$, and specific star formation rate log(sSFR) < -9.7. Then, it was identified as a quiescent candidate from the *UVJ* diagnostic and by the strong Balmer/4000 Å break. Finally, D. Marchesini et al. (2023) confirmed its quiescent nature by fitting JWST/NIRCam photometry and NIRISS grism slitless spectroscopy. Follow-up JWST observations provided further photometric and spectroscopic data, as detailed below. We show the NIRSpec spectrum and the Hubble Space Telescope (HST) +NIRCam photometry of GLASS-180009 in Figure 1. In Appendix A, we show that the spectrum does not suffer wavelength calibration issues, and describe how we rescaled it to the photometry.

We took the photometric data from the JWST UNCOVER Treasury Program (R. Bezanson et al. 2024) and the Medium Bands, Mega Science survey (hereafter MegaScience; K. A. Suess et al. 2024). The combined catalog, described in J. R. Weaver et al. (2024), includes imaging for all 20 NIRCam wide and medium bands. Specifically, UNCOVER obtained JWST/NIRCam broadband imaging of the A2744 cluster in the NIRCam F115W, F150W, F200W, F277W, F356W, F410M, and F444W broad bands, and MegaScience imaged the same footprint in two additional broad bands, F070W and F090W, and the medium bands F140M, F162M, F182M, F210M, F250M, F300M, F335M, F360M, F430M, F460M, and F480M. The reduction pipelines are presented in R. Bezanson et al. (2024) and K. A. Suess et al. (2024). Additionally, the catalog includes HST observations in the F435W, F606W, F814W, F105W, F125W, F140W, and F160W filters. Throughout this work, we adopt the data products of Data Release 4 (DR4), which includes corrections for gravitational lensing effects (L. J. Furtak et al. 2023) with updated spectroscopic redshifts (S. H. Price et al. 2025). The catalog ID for GLASS-180009 is 27482.

We considered NIRSpec spectroscopic observations with the high-resolution gratings ($R \sim 2700$) of JWST from GLASS, described in S. Mascia et al. (2024), and with the PRISM ($R \sim 100$) from UNCOVER, described in S. H. Price et al. (2025). In this work, we used the reduced data from the DAWN JWST Archive (DJA; G. Brammer 2022).[19] The median signal-to-noise ratios (S/Ns) of the high-resolution gratings are ∼5, 18, and 20 Å^{-1}, for G140H/F100LP, G235H/F170LP, and G395H/F290LP, respectively.

We derive the effective radius of the major axis (R_e) and Sérsic index (n) by fitting the NIRCam imaging in the F277W filter using `pysersic` (I. Pasha & T. B. Miller 2023), as described in Appendix B, for which we estimate $R_e = 1.05^{+0.01}_{-0.01}$ kpc and $n = 2.15^{+0.01}_{-0.01}$. Using early data from GLASS, D. Marchesini et al. (2023) estimated a stellar mass of $\log(M_*/M_\odot) = 10.59^{+0.11}_{-0.05}$ (corrected for magnification effects), assuming a G. Chabrier (2003) stellar IMF. Note that in Appendix C we refit the stellar mass using both the spectrum and the additional photometric data, and find a consistent value for the stellar mass ($4.6^{+0.1}_{-0.1} \times 10^{10}\,M_\odot$).

3. Analysis

3.1. Integrated Stellar Velocity Dispersion

We estimated the stellar velocity dispersion (σ_*) from the full spectral fitting of the high-resolution spectrum using

[19] Available from https://dawn-cph.github.io/dja/.

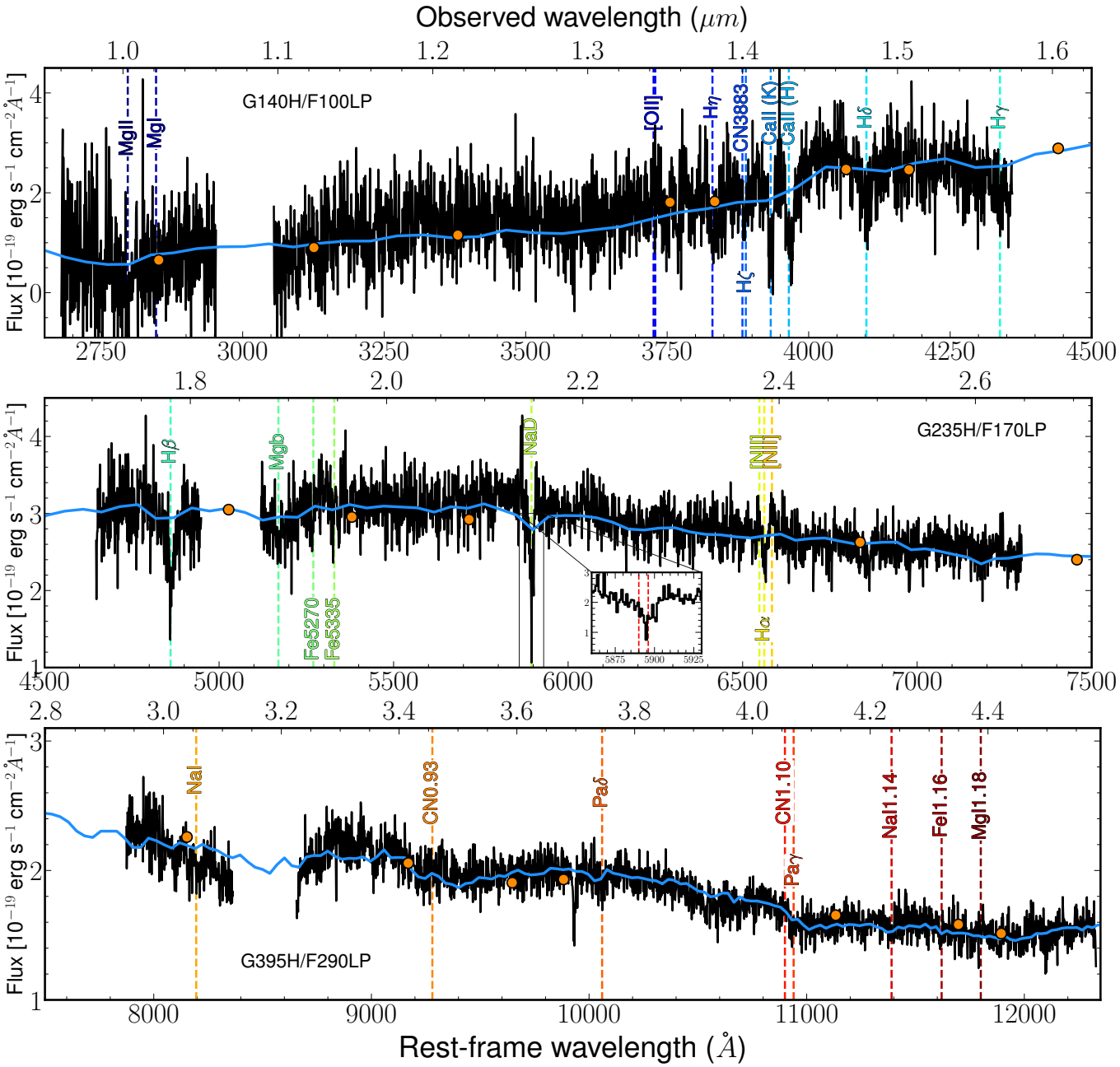

Figure 1. JWST spectrum and photometry of GLASS-180009. The top, middle, and bottom panels show the wavelength regions corresponding to the G140H/F100LP, G235H/F170LP, and G395H/F290LP gratings, respectively. In each panel, the grating and PRISM spectra are plotted with black and blue curves, respectively, while the photometric data are shown as orange circles. The two spectra are rescaled to the photometry. The missing wavelength regions of the grating spectrum are the detector gaps. The main absorption and emission lines detected are highlighted with dashed vertical lines. In the middle panel, we show a zoom in of the NaD absorption feature from the grating spectrum. The vertical red dashed lines show the expected wavelengths of the two Na I absorption lines at $\lambda\lambda$5890, 5896, while the observed features are evidently redshifted.

pPXF (M. Cappellari 2023). As input templates, we considered the EMILES simple stellar population (SSP) models (A. Vazdekis et al. 2016; see the next section for a more detailed description) and broadened them to match the resolution of the grating spectra. We excluded from the fit wavelengths below 1.2 μm (∼3500 Å rest frame), due to the low S/N (<3 Å^{-1}). We also mask NaD since it mostly originates in the neutral gas inflow, as discussed below. We then performed a first fit of the spectrum with pPXF and computed the standard deviation of the residuals ($\sigma_{\rm std}$). Following this, we masked all the spectral pixels deviating more than $3\sigma_{\rm std}$ from the previous best fit and performed a second fit. We consider the results of this second fit as our best-fitting solutions.

To estimate the errors, we performed a wild bootstrapping of the residuals by resampling the best-fitting spectrum with the noise Gaussianly redistributed from the residuals. For each iteration, we performed 100 realizations and considered the standard deviation as the relative error. To account for errors due to the correlation in wavelength, in each iteration we shuffled residuals over windows about 500 Å wide. All the fits were performed including additive polynomials of degree 10 to account for possible bad subtraction of the background. We present the results of our kinematic fits in Section 4.1.

3.2. Stellar Population Modeling

We estimated the stellar population properties from the full spectral fitting using pPXF fed with the EMILES models. Specifically, we adopted the "baseFe" models computed with BaSTI isochrones (A. Pietrinferni et al. 2004) and a G. Chabrier (2003) IMF. We considered models with ages $\leqslant$2.5 Gyr, since the age of the Universe at the redshift of the galaxy is $\simeq$2.4 Gyr, and older than 0.07 Gyr, because the EMILES models with younger ages have lower accuracy (A. Vazdekis et al. 2016). In Appendix C, we show that including models with younger ages does not change the results. For the metallicity ([M/H]), we considered models with values between -1.79 and $+0.26$ dex.

We set up our fits as follows. We limited the fit to the rest-frame wavelength region 3500–12300 Å, also excluding the NaD line, and fixed the velocity dispersion of the stars to our best-fitting σ_* (Section 4.1). We simultaneously fit, as independent kinematic components, the stars and the gas emission lines, parameterized as Gaussians. In particular, we fit the [O II] doublet ($\lambda = 3726, 3728$ Å), He I ($\lambda = 5877$ Å) the [O I] doublet ($\lambda = 6302, 6366$ Å), the [N II] doublet ($\lambda = 6718, 6733$ Å) and the Balmer lines.[20] For the stellar component, we also fit a D. Calzetti et al. (2000) reddening curve.

We obtained the pPXF best-fitting model as follows. We performed a first fit of the spectrum and computed the standard deviation of the residuals ($\sigma_{\rm std}$). We then performed a second fit, masking spectral pixels that deviated by more than $3\sigma_{\rm std}$ from the previous best fit. We consider the results of this second fit as our best-fitting solutions. We calculate the mass-weighted age and metallicity as

$$\log_{10}\mathrm{Age} = \frac{\sum_i w_i \log_{10}\mathrm{Age_i}}{\sum_i w_i}, \tag{1a}$$

$$[\mathrm{M/H}] = \frac{\sum_i w_i [\mathrm{M/H}]_i}{\sum_i w_i}, \tag{1b}$$

where w_i is the best-fitting weight of the ith input template, and the sums are performed on all the input templates.

To estimate the errors of age, metallicity, and dust attenuation, we performed a wild bootstrapping of the residuals. Toward this aim, we performed 100 realizations of each spectrum, shuffling the residuals over windows $\sim$500 Å wide each time to account for wavelength-correlated errors, and then Gaussianly redistributed (i.e., added) the shuffled residuals to the best-fitting spectrum. For each realization, we estimated the stellar population parameters and took the standard deviations of all the realizations as their errors.

In addition to the stellar population parameters, we recover the SFH of GLASS-180009 in a nonparametric way using the same setup and methods described above, but allowing for regularization during the fit (M. Cappellari 2017). The SFH is then calculated as the cumulative sum of the best-fitting mass weights.

We show the best-fitting spectrum and the SFH in Figures 2 and 3, respectively. We present the results in Section 4.2. The best-fitting stellar population properties are reported in Table 1.

3.3. Modeling the NaD Absorption Lines Tracing the Neutral Gas Inflow

Inspection of the Na I doublet at $\lambda\lambda$5890, 5896 (Figure 1) shows clear redshifted absorption which is caused by neutral gas inflow. We then derived the properties of the inflowing gas by modeling the NaD absorption lines with VoigtFit (J.-K. Krogager 2018). The code models the lines with a Voigt profile and fits the velocity, v, the broadening due to thermal and turbulent motions, b, and the column density of the absorber, $N_{\rm NaI}$. Before fitting the observed spectrum, we corrected it for stellar absorption by subtracting the pPXF best-fitting stellar population model spectrum. We note that we do not detect any He I emission (see Table 1), which could in principle affect the Na absorption features.

To assess the best-fitting parameters and errors, we used a Bayesian Markov Chain Monte Carlo (MCMC) approach. We implemented MCMC sampling using the ensemble sampler implemented in emcee (D. Foreman-Mackey et al. 2013) to estimate the posterior probability distribution of the model parameters. We initialized the sampler with 50 walkers and ran the MCMC chains for 5000 steps, discarding the first 1500 steps as burn-in. The likelihood function was defined as $\ln\mathcal{L} = -\frac{1}{2}\chi^2$, where χ^2 is returned by VoigtFit for each given set of input parameters, v, b, and $\log(N_{\rm NaI})$. We adopted flat priors for all parameters. We consider the best-fitting parameters of the marginalized posterior distributions as the median values, and the 16th and 84th percentiles as the errors. We show the best fit of the NaD absorption features in Figure 4, and report the best-fitting parameters in Table 2. We present our results in more detail in Section 4.3.

4. Results

4.1. Dynamical Properties

From the kinematic fits, we find a best fit of $\sigma_* = 233 \pm 26\,\mathrm{km\,s^{-1}}$. To have an independent check and to account for possible wavelength calibration issues among the different NIRSpec gratings (e.g., F. D'Eugenio et al. 2025), we reestimated σ_* by fitting only the G140H/F100LP spectrum with the MILES stars (P. Sánchez-Blázquez et al. 2006) using the same methods described in Section 3.1, and found a consistent best fit of $\sigma_* = 227 \pm 18\,\mathrm{km\,s^{-1}}$. Finally, we note that we find a consistent velocity dispersion when fitting the spectrum with Bagpipies (see Appendix C). We adopt the σ_* derived from the fit of the entire spectrum with pPXF fed with the EMILES models as our reference value.

From the stellar velocity dispersion, we infer the dynamical mass of GLASS-180009 to be $M_{\rm dyn} = k(n) R_e\, \sigma_e^2/G \simeq 9.9 \times 10^{10}\, M_\odot$, assuming $k(n) \approx 8.87 - 0.83\,n + 0.024\,n^2$ (M. Cappellari et al. 2006) and $\sigma_e \approx \sigma_*$.[21] This implies a dark matter fraction $M_{\rm DM}/M_{\rm dyn} = 1 - M_*/M_{\rm dyn} \simeq 0.61$, namely a factor of $\sim$1.5 larger than the stellar mass, which is unusually large at $z > 2$ (e.g., J. van de Sande et al. 2013; A. Beifiori et al. 2014; C. Tortora et al. 2014;

[20] We verified that other typical emission lines falling in the observed wavelength range (e.g., [Ne II], [S II], etc.) are undetected or have relative errors larger than 100%.

[21] This is justified because the effective radius of GLASS-180009, $R_e \simeq 0.13''$, is comparable (lower than) the (circularized) aperture of the microshutter $R_{ap} \simeq 0.17''$, so we do not apply any aperture correction (I. Jorgensen et al. 1995; M. Cappellari et al. 2006).

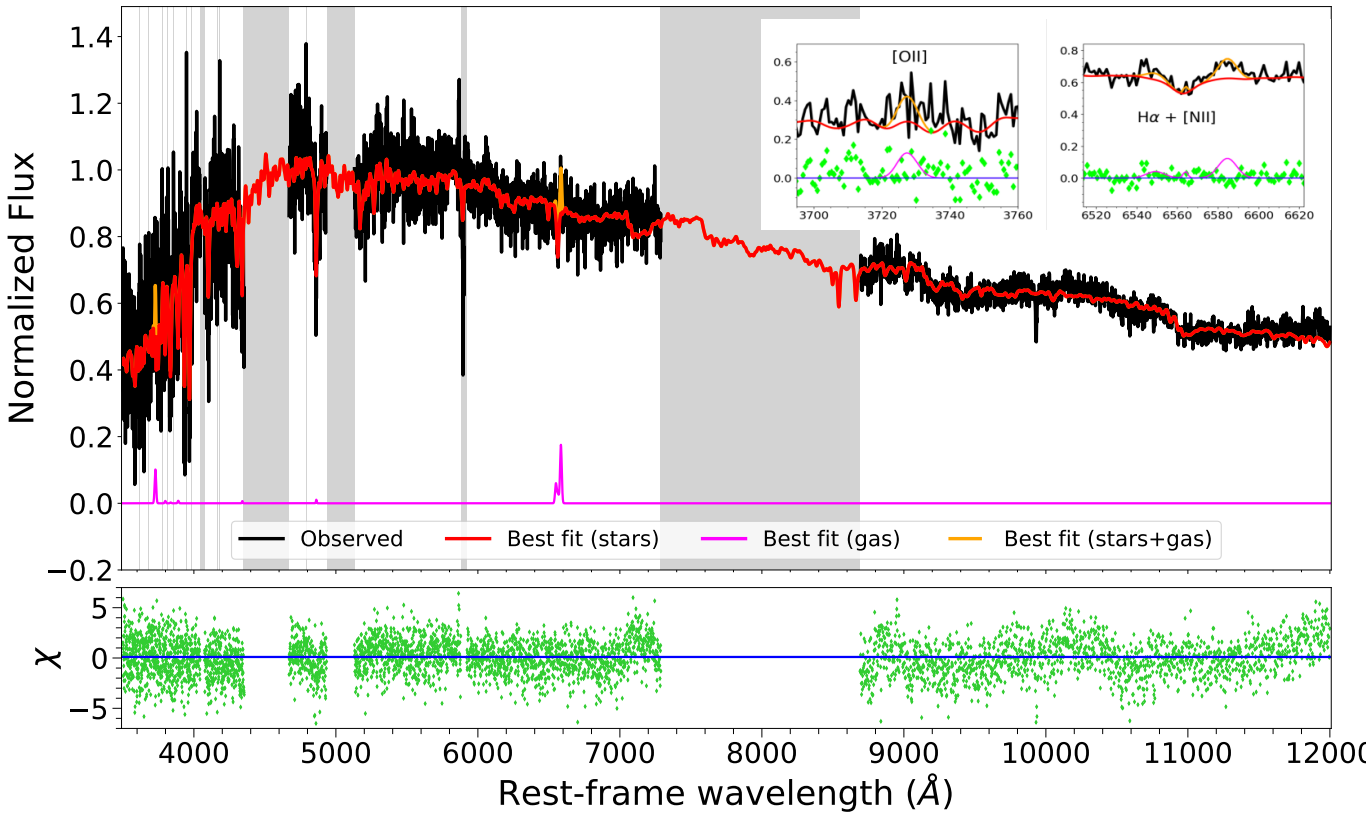

Figure 2. Best fit of the JWST high-resolution spectrum of GLASS-180009. Top panel: the black curve is the observed spectrum, the red curve is the best-fit stellar spectrum, the magenta curve is the best fit of the gas emission lines, the orange curve is the combined best fit of the stars and gas, and the gray shaded regions are the spectral regions masked during the fit. The two insets in the upper-right corner show zoom ins of the [O II] and Hα+[N II] line fits. Bottom panel: the green diamonds, χ, are the difference between the observed spectrum and best-fit model spectrum divided by the errors. The blue horizontal line is the median χ value.

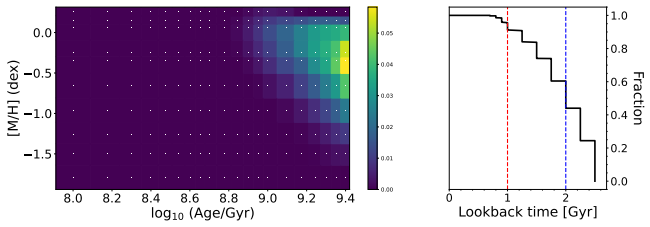

Figure 3. Left panel: map of the mass weights assigned by pPXF to each input template of given age and metallicity from the regularized fit. Right panel: fraction of mass weight as a function of lookback time. The SFH is calculated as the cumulative sum of the weights. The red and blue lines indicate t_{50} and t_{95}, respectively.

M. R. Lovell et al. 2018; J. T. Mendel et al. 2020). Alternatively, under the assumption of the galaxy being baryon dominated within the effective radius, a comparison between the dynamical and the stellar masses suggests that the IMF is more bottom-heavy than a G. Chabrier (2003) IMF. Assuming a variation of the IMF with velocity dispersion (e.g., M. Cappellari et al. 2012; F. La Barbera et al. 2013; C. Conroy et al. 2013), we would need a Salpeter-like IMF to have $M_* \approx M_{\rm dyn}$. This is in agreement with recent results from M. Slob et al. (2025) based on a sample of 15 massive quiescent galaxies at $z \sim 2$. However, we note that the Sérsic index of GLASS-180009 is relatively low ($n = 2.15$) compared to the typical values of local quiescent galaxies with comparable σ_* and mass (e.g., H. J. Zahid & M. J. Geller 2017). This might indicate the presence of stellar rotation (as also found in M. Slob et al. 2025) that would account for part of the broadening. In this way, σ_* and $M_{\rm dyn}$ might be overestimated. Furthermore, we note that a variation of the IMF with the radius can have a significant impact on the estimate of M_* and $M_{\rm dyn}$ (I. Martín-Navarro et al. 2015; P. van Dokkum et al. 2017; F. La Barbera et al. 2019; M. Bernardi et al. 2023). Finally, we note that the relation between the dynamical mass and velocity dispersion we adopted is calibrated on local galaxies and might be different at high z.

4.2. Stellar Population Properties and SFH

From the fit of the stellar population properties, we find that GLASS-180009 has an age of 1.74 ± 0.18 Gyr, a subsolar metallicity $[{\rm M/H}] = -0.26 \pm 0.09$ dex, and a dust attenuation $A_V = 0.24 \pm 0.06$ mag. The recovered SFH suggests that the galaxy formed 50% and 95% of its mass at lookback times $t_{50} = 2.00 \pm 0.25$ Gyr and $t_{95} = 1.00 \pm 0.15$ Gyr, corresponding to $z_{50} = 11^{+18}_{-3}$ and $z_{95} = 4.3^{+0.3}_{-0.4}$, respectively, and then quenched without any significant recent SF. We note that, according to its SFH, GLASS-180009 is an "ancient" galaxy, having formed $\geqslant$50% of its mass at $z_{50} \geqslant 11$, similar to other galaxies recently discovered with JWST and possibly challenging ΛCDM (A. C. Carnall et al. 2024; A. de Graaff et al. 2025; K. Glazebrook et al. 2024; I. McConachie et al. 2025), although in this case the mass at z_{50} is not as high.

In Appendix C, we test the reliability of the derived stellar population properties and SFH. In particular, we fit the spectrum using the G. Bruzual & S. Charlot (2003) models (updated to version 2016; hereafter BC16) to consider the effect of including models with very young ages (down to

Table 1
Stellar Population Properties and Emission Lines Estimated from the Full Spectral Fitting with `pPXF` Adopting the EMILES Models

Parameter/Unit	Value
σ_*/km s^{-1}	233 ± 26
Age/Gyr	1.74 ± 0.18
Metallicity/dex	−0.26 ± 0.09
A_V/mag	0.24 ± 0.06
F(Hα)/10^{-20} erg s^{-1} cm^{-2}	3.2 ± 2.2
F(Hβ)/10^{-20} erg s^{-1} cm^{-2}	1.4 ± 1.2
F(Hγ)/10^{-20} erg s^{-1} cm^{-2}	0.9 ± 0.8
F([O II])/10^{-19} erg s^{-1} cm^{-2}	4.1 ± 1.4
F([O I])/10^{-19} erg s^{-1} cm^{-2}	1.6 ± 0.5
F([N II])/10^{-19} erg s^{-1} cm^{-2}	6.1 ± 0.8
F(He I)/10^{-20} erg s^{-1} cm^{-2}	0.0 ± 0.8
SFR(Hα)/$M_\odot$ yr^{-1}	0.02 ± 0.01
SFR([O II])/$M_\odot$ yr^{-1}	0.19 ± 0.07
t_{50}/Gyr	2.00 ± 0.25
t_{95}/Gyr	1.00 ± 0.15

Note. Age and metallicity are mass-weighted. Most of the other Balmer lines are detected but are very low and consistent with zero flux, so we do not report them here. The He I emission is not detected; we explicitly report it here because this emission line would affect the NaD measurement, if detected. The star formation rate (SFR) values are derived from the emission lines (Section 4.2). The values of t_{50} and t_{95} are derived from the SFH, reconstructed from the regularized fits.

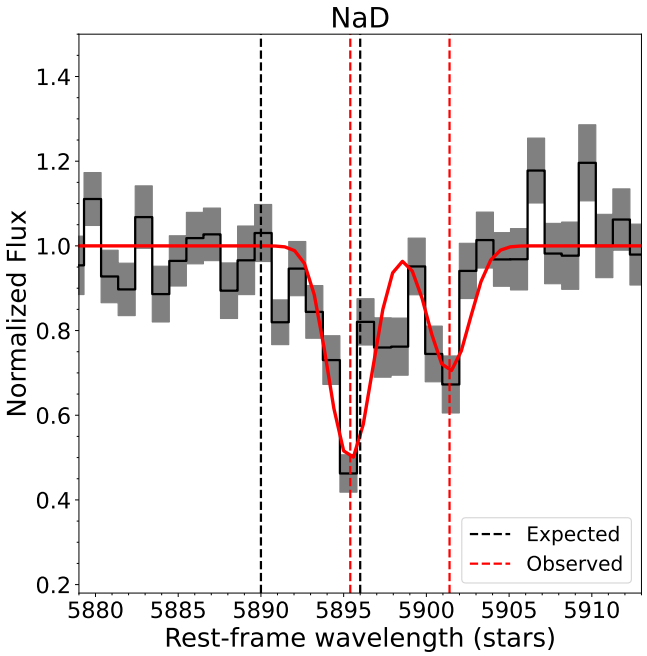

Figure 4. NaD absorption features of the inflowing neutral gas. The black curve is the observed spectrum corrected for the stellar continuum. The gray regions indicate the errors on the flux. The red curve is the best-fitting solution of `VoigtFit`. The black (red) vertical lines indicate the wavelengths of the two expected (observed) Na I absorption lines.

Table 2
Properties of the Inflowing Neutral Gas Estimated from the Fit of the Na I Doublet at $\lambda\lambda$5890, 5896

Parameter/Unit	Value
v/km s^{-1}	278^{+79}_{-79}
b/km s^{-1}	78^{+26}_{-25}
$\log(N_{\rm NaI})$/cm^{-2}	$13.02^{+0.03}_{-0.03}$
$\log(N_{\rm H})$/cm^{-2}	$20.66^{+0.03}_{-0.03}$
$M_{\rm in}/M_\odot$	$1.6^{+0.1}_{-0.1} \times 10^8$
$\dot{M}_{\rm in}/M_\odot$ yr^{-1}	19^{+6}_{-7}

Note. Errors take into account uncertainties in the redshift and the spectral sampling. $\log(N_{\rm H})$ is calculated using Equation (2). $M_{\rm in}$ and $\dot{M}_{\rm in}$ are calculated using Equations (3).

0.1 Myr). In addition, we test the reliability of our fitting methods by comparing our results with those obtained from `Bagpipes` (A. C. Carnall et al. 2018). In summary, we find that the BC16 models favor solutions with younger ages and higher metallicities than the EMILES models. However, this difference is not due to the inclusion of young models, as they do not contribute to the best-fitting model spectrum, but rather to the wavelength region fitted and to differences in the model libraries. Crucially, we find that the quenching time, t_{95}, is the same. We find consistent results when fitting the spectrum with `Bagpipes`.

We derive the current star formation rate (SFR) from the Hα and [O II] emission lines as follows. First, we correct the measured fluxes for dust attenuation as $F_{\rm corr} = F \times e^{\tau_\lambda}$, with $\tau_\lambda = A_\lambda/1.086$ and $A_\lambda = k_\lambda A_V/R_V$, where k_λ is the reddening curve for the gas, for which we assume a D. Calzetti et al. (2000) law with $R_V = 4.05$ and $A_V = 0.24$ mag, as estimated from the fit. Then, we calculate the luminosities of the two lines as $L = 4\pi d_L^2 \times F_{\rm corr}$, where $d_L = 2.2 \times 10^4$ Mpc is the luminosity distance, and find $L_{\rm H\alpha} \simeq 2.3 \times 10^{39}$ erg s^{-1} and $L_{\rm [O\,II]} \simeq 2.9 \times 10^{40}$ erg s^{-1}. Thus, we estimate the SFR from Hα using Equation (2) of R. C. Kennicutt (1998) as SFR (Hα) $= 7.9 \times 10^{-42}\, L_{\rm H\alpha} = 0.02 \pm 0.01\, M_\odot$ yr^{-1}, and from [O II] using Equation (4) of L. J. Kewley et al. (2004) as SFR([O II]) $= 6.58 \pm 1.65 \times 10^{-42}\, L_{\rm [O\,II]} = 0.19 \pm 0.07\, M_\odot$ yr^{-1}, assuming a G. Chabrier (2003) IMF.

We note that these values are upper limits to the actual SFR. In particular, the [OII] emission could also be due to the presence of evolved stars, such as post-asymptotic giant branch stars, or shocks (e.g., M. A. Dopita & R. S. Sutherland 1995; R. Cid Fernandes et al. 2011). This could be probed, for instance, with the [O III] line at 5007 Å, which could be used to derive the ionization level of the nebular emission and discriminate between low and high excitation. However, [O III] is not measurable from the high-resolution spectrum because it falls within the detector gaps. From the PRISM spectrum, which covers the wavelength of the [O III] line, we do not detect any emission either; nor is it detected in the NIRISS slitless spectrum taken from D. Marchesini et al. (2023). Assuming that the nondetection in the PRISM spectrum is due to its low resolution spreading out the flux over the FWHM, we can estimate an upper limit to the flux of [O III].[22] We estimate $F_{\rm min}$([O III]) $= 5.3 \times 10^{-20}$ erg s^{-1} cm^{-2}, above which we would detect the

[22] The minimum flux integrated over the resolution element, $\Delta\lambda = \lambda/R$, required to have a 1σ detection can be calculated as $F_{\rm min} = f_\lambda \cdot \Delta\lambda = \sigma_\lambda \cdot \Delta\lambda$, where $\sigma_\lambda = \sigma_{\rm pix} \cdot \sqrt{N_{\rm pix}} = \frac{f_c}{\rm S/N} \cdot \sqrt{\frac{\Delta\lambda}{\delta\lambda}}$ is the noise within the resolution element, with f_c and $\delta\lambda$ being the flux of the continuum and the spectral sampling, respectively.

emission. This implies an upper limit of $\log([\mathrm{OIII}]/\mathrm{H}\beta) \simeq 0.6$ dex, which, combined with the relatively high ratios $\log([\mathrm{NII}]/\mathrm{H}\alpha) \simeq 1.3$ dex and $\log([\mathrm{O\,I}]/\mathrm{H}\alpha) \simeq 0.7$ dex, would place this galaxy in the LI(N)ER region of the Baldwin–Phillips–Terlevich diagram (J. A. Baldwin et al. 1981; L. J. Kewley et al. 2006; F. Belfiore et al. 2016).

Given the stellar mass and SFR of GLASS-180009, we derive an upper limit to the sSFR of $\mathrm{SFR}([\mathrm{OII}])/\mathrm{M}_* = 0.5 \pm 0.1 \times 10^{-11}\,\mathrm{yr}^{-1}$, which is more than 1 dex lower than the limit defined by A. Gallazzi et al. (2014) for local galaxies, $\mathrm{sSFR} < 0.2/t_{\mathrm{U}}(z) \simeq 8 \times 10^{-11}$, where $t_{\mathrm{U}} = 2.4$ Gyr is the age of the Universe at the galaxy's redshift. This confirms the quiescent nature of GLASS-180009. We also note that we measure a (dust-corrected) value for the spectral index D_n4000 (M. L. Balogh et al. 1999) of 1.47 ± 0.02, which is typical of poststarburst galaxies that do not have significant SF (G. Kauffmann et al. 2003; V. Wild et al. 2009; K. D. French et al. 2018).

Finally, we mention that the quality of the spectra is not sufficiently high to robustly constrain the elemental abundances of GLASS-180009. Furthermore, because of the relatively young age of this galaxy, the effect of elemental abundances is intrinsically hard to measure. As described in Appendix D, we attempted to constrain the abundance of [Mg/Fe], for which we estimate $[\mathrm{Mg/Fe}] = 0.11^{+0.15}_{-0.13}$ dex, suggesting possible α-enhancement.

4.3. Properties of the Inflowing Gas

From the fit of the Na I doublet at $\lambda\lambda$5890, 5896 with `VoigtFit` (Section 3.3), we estimate $v = 278^{+79}_{-79}$ km s^{-1}, $b = 78^{+26}_{-25}$ km s^{-1}, and $\log(N_{\mathrm{NaI}}/\mathrm{cm}^2) = 13.02^{+0.03}_{-0.03}$.[23] In Figure 4, we show the best-fit `VoigtFit` profile.

Since the best-fitting model does not account for possible Na enhancement or the presence of neutral gas in the galaxy, we tested these effects by manually deepening the NaD stellar features in the best-fit `pPXF` spectrum. To do this, we used the Na-enhanced models of C. Conroy et al. (2018) with $[\mathrm{Na/H}] = +0.3$ dex, interpolated at the same age and metallicity as our best-fitting values. We then subtracted the Na-enhanced spectrum from the observed continuum and ran `VoigtFit` as described in Section 3.3. As a result, we find a lower value for the column density of Na I, $\log(N_{\mathrm{NaI}}/\mathrm{cm}^2) = 12.94^{+0.04}_{-0.04}$, while v and b are consistent. However, this small difference does not qualitatively change our results.

We note that the rest-frame JWST high-resolution spectrum also covers the Mg II doublet at $\lambda\lambda$2796, 2803 and the Ca II K line doublet at 3934 Å, two other tracers of the neutral gas (e.g., C. Liboni et al. 2025; P.-F. Wu 2025). In the former case, a shift toward redder wavelengths is recognizable, but we could not perform a robust fit because of the low S/N (~ 2 Å^{-1}). In the latter case, the shift is not easily distinguishable because the gas absorption falls within the stellar feature. We mention that, by correcting for stellar absorption, we indeed found residuals consistent with the presence of an inflow in Ca II K. However, the stellar Ca II K absorption is sensitive to the Ca abundance and is affected by Hϵ, and as we cannot safely constrain them with current data, we did not attempt to derive the properties of the inflowing gas from the Ca II K line.

[23] The reported errors were propagated to account for uncertainties in the redshift and spectral sampling.

Following D. S. Rupke & D. B. Sanders (2005), S. Veilleux et al. (2020), P.-F. Wu (2025), and F. Valentino et al. (2025), we converted the $\log(N_{\mathrm{NaI}})$ estimated from NaD into hydrogen column density using the following equation:

$$\log(N_{\mathrm{H}}) = \log(N_{\mathrm{NaI}}) - \log(X^0_{\mathrm{Na}}) - A_{\mathrm{Na}} - B_{\mathrm{Na}}, \tag{2}$$

where $X^0_{\mathrm{Na}} \equiv N_{\mathrm{NaI}}/N_{\mathrm{Na}}$ is the fraction of Na that is neutral, A_{Na} is the abundance of Na relative to H in the gas phase, and B_{Na} is the level of depletion of Na into dust. As described in S. Veilleux et al. (2020), and following P.-F. Wu (2025) and F. Valentino et al. (2025), we adopt a neutral gas fraction $X^0_{\mathrm{Na}} = 0.1$ (G. M. Stokes 1978), a Milky Way–like sodium abundance $A_{\mathrm{Na}} = -5.69$, and depletion $B_{\mathrm{Na}} = -0.95$ (B. D. Savage & K. R. Sembach 1996). Thus, we estimate $\log(N_{\mathrm{H}}/\mathrm{cm}^2) = 20.66^{+0.03}_{-0.03}$.

Then, following D. S. Rupke & D. B. Sanders (2005), R. L. Davies et al. (2024), P.-F. Wu (2025), and F. Valentino et al. (2025), we estimate the inflowing mass and rate, assuming a simple spherical thin-shell model, as

$$M_{\mathrm{in}} = 1.4\, m_p\, \Omega\, N(\mathrm{H})\, R^2_{\mathrm{in}}, \tag{3a}$$

$$\dot{M}_{\mathrm{in}} = 1.4\, m_p\, \Omega\, N(\mathrm{H})\, R_{\mathrm{in}}\, v_{\mathrm{in}}, \tag{3b}$$

where m_p is the mass of the proton, Ω is the solid angle subtended by the inflow, R_{in} is the shell radius, and v_{in} is the velocity of the inflow from the best fit of `VoigtFit`. Following the above-mentioned papers, we set $\Omega = 0.45 \times 4\pi$, which assumes a randomly oriented inflow (P.-F. Wu 2025), and $R_{\mathrm{in}} = 2 \times R_e$, which assumes a covering fraction for Na I of ≈ 1 and that the physical extent of the inflowing gas is as extended as (half of) the stellar light. We estimate an inflowing mass $M_{\mathrm{in}} = 1.6^{+0.1}_{-0.1} \times 10^8\, M_\odot$ and rate $\dot{M}_{\mathrm{in}} = 19^{+6}_{-7}\, M_\odot\,\mathrm{yr}^{-1}$.

We caution that these assumptions represent the main source of uncertainty in our analysis. For instance, studies based on outflows show that the covering fraction of Na I is typically lower than 1 and generally varies in the range $\sim$0.3–1, depending on the source of the outflow (D. S. Rupke & D. B. Sanders 2005; C. L. Martin & N. Bouché 2009; K. H. R. Rubin et al. 2014; R. L. Davies et al. 2024). Furthermore, NaD is expected to be clumpy (e.g., N. Roy et al. 2021). Therefore, our assumptions about the properties and geometry of the neutral gas could lead to an overestimate of the inflowing mass and rate. On the other hand, both observational (e.g., D. S. Rupke & D. B. Sanders 2005; C. L. Martin & N. Bouché 2009) and theoretical (e.g., N. Murray et al. 2007; P. Richter et al. 2011) studies show that Na I traces only the coldest and densest gas, resulting in systematically lower inferred hydrogen column densities compared to estimates based on other lines such as Mg II and Fe II, which trace more diffuse or ionized phases. For example, F. Valentino et al. (2025) estimated values of $\log(N_{\mathrm{H}}) \sim 1$ dex higher when estimated from Mg II and Fe II compared to Na I. This implies that we may be underestimating $\log(N_{\mathrm{H}})$, and thus M_{in} and $\dot{M}_{\mathrm{in}}$. Finally, the assumptions adopted in Equation (2) also affect the estimates of N_{H}, although L. Moretti et al. (2025) recently confirmed the validity of these assumptions for one massive quiescent galaxy at $z \sim 2$. In summary, our estimates have intrinsic uncertainties that can only be reduced with targeted observations of the neutral gas to robustly constrain the hydrogen column density and the geometry of the inflow. However, they allow us to directly compare our results with other works in the literature.

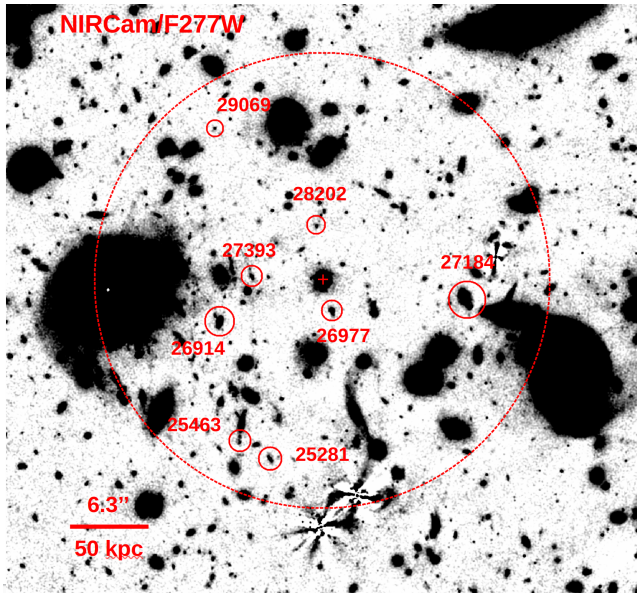

Figure 5. NIRCam imaging of GLASS-180009 in the F277W filter. The scale is shown in the lower-left corner. The target galaxy is marked with a cross. The big dashed circle demarcates a surrounding region of about 150 kpc at the galaxy's redshift. The small circles highlight the eight galaxies within the 150 kpc projected distance having redshifts comparable to that of our target galaxy. The UNCOVER catalog ID of each galaxy is reported close to each circle.

5. Discussion

In the previous sections, we have shown that GLASS-180009 presents an evident redshift of the NaD lines, indicating the presence of neutral gas inflow, for which we derived the mass and rate. Despite the gas inflow, the galaxy remains quiescent, with no evidence of any significant SF burst during the last ∼1 Gyr according to its SFH. In this section, we discuss the possible sources of the inflow and the potential reasons why it does not lead to the ignition of SF.

5.1. The Source of the Inflowing Neutral Gas

Different sources of neutral gas may be responsible for the observed inflow, including satellite galaxies through tidal streams or mergers, the IGM or cosmic filaments, and galactic fountains (A. Fox & R. Davé 2017). Since GLASS-180009 is residing in an overdensity (R. Pan et al. 2025; P. J. Watson et al. 2025), satellite galaxies represent viable sources for the neutral gas. To test this hypothesis, we checked the environment of GLASS-180009 in the JWST imaging. In Figure 5, we show a 50″ × 50″ (about 400 × 400 kpc) zoom-in image of the NIRCam F277W filter from UNCOVER centered at our target galaxy. We looked for close companions of GLASS-180009 in the UNCOVER/MegaScience catalog by selecting galaxies with photometric redshifts between 2.6 and 2.8 (i.e., approximately ±0.1 from our target) and with projected distances within 150 kpc. We found 10 galaxies surrounding GLASS-18009. We compared the photometric redshifts of these galaxies with those in the NIRISS catalog (P. J. Watson et al. 2025) and confirmed the proximity only for two galaxies (GLASS IDs 25281 and 26914), while two other galaxies have significantly different redshifts, and so were excluded; the remaining six galaxies do not have redshift measurements in the NIRISS catalog. We show the eight surrounding galaxies in Figure 5. From the DR4 catalog of the photometric SED fitting (B. Wang et al. 2024), we found that all these galaxies have low stellar masses, $\log_{10}(M_*/M_\odot) = 6.8 - 9.2$, young ages, 0.1–1 Gyr, and relatively high sSFRs, $\log_{10}(\mathrm{sSFR}/\mathrm{Gyr}^{-1}) = 1 - 10$. Among these, only two galaxies, 26977 and 26914, have a stellar mass higher than the mass of the inflowing gas, $10^{8.2}\,M_\odot$. In particular, 26977 appears as the closest surrounding galaxy, having a projected distance $\lesssim$20 kpc. If the neutral gas inflow is a consequence of an ongoing wet minor merger, then this galaxy represents the best source candidate. If instead it is due to tidal streams, it is likely that more than one galaxy is contributing to the total mass of the inflowing gas. We note that R. L. Davies et al. (2024) found a passive galaxy with evidence of neutral gas inflow, highlighting the presence of a close companion that is possibly fueling the inflow, similar to our case.

To further investigate the environment, we considered Atacama Large Millimeter/submillimeter Array (ALMA) observations of the A2744 cluster at 244–274 GHz, recently released by S. Fujimoto et al. (2025). We show the ALMA observations of the same sky region shown in Figure 5 in Appendix E (Figure 12). Unfortunately, these observations are dominated by noise, and do not show any clear detection of gas around GLASS-180009 or the surrounding galaxies. Therefore, targeted observations for neutral gas are needed to further address the origin of the inflow. This would also allow us to probe the IGM or cosmic filaments as other sources of the inflow, which cannot be ruled out on the basis of current data.

Finally, we consider the possibility that the inflow originates from a galactic fountain, i.e., from recycled material of SF. There are two main arguments against the galactic fountain explanation. First, they are usually associated with significant SF activity. Both observations (e.g., A. J. Fox et al. 2019) and models (e.g., A. Marasco et al. 2012) indicate that the rate of neutral gas inflow due to galactic fountains is of the same order of the SFR. For example, R. L. Davies et al. (2024) recently reported two star-forming galaxies with evidence of neutral gas inflows (having masses and rates very similar to those of our target galaxy), potentially indicating galactic fountains (see also K. H. R. Rubin et al. 2012; A. Weldon et al. 2023). However, the SFR ($\leqslant 0.2\,M_\odot\,\mathrm{yr}^{-1}$) of GLASS-180009 is at least 2 dex lower than the mass-accretion rate of the gas ($\sim 20\,M_\odot\,\mathrm{yr}^{-1}$). Even assuming a delayed reaccretion of the ejected material, typical galactic fountain return timescales are of the order of a few hundreds of Myr (B. D. Oppenheimer & R. Davé 2008; E. Spitoni et al. 2009, 2013; A. J. Fox et al. 2019; R. J. J. Grand et al. 2019), while GLASS-180009 stopped forming stars ∼1 Gyr before observations according to its SFH. Second, observations indicate that galactic fountains typically exhibit hydrogen column densities of $\log(N_{\mathrm{H\,I}}/\mathrm{cm}^{-2}) \sim 18$–$20$ and sodium column densities of $\log(N_{\mathrm{Na\,I}}/\mathrm{cm}^{-2}) \sim 12$ (e.g., N. Ben Bekhti et al. 2008; M. E. Putman et al. 2012; K. H. R. Rubin et al. 2022), i.e., at least 1 dex lower than the densities we estimated. Therefore, it is unlikely that the neutral gas inflow we detect in GLASS-180009 is due to a galactic fountain.

5.2. The Fate of the Inflowing Gas

An inflow of neutral gas in galaxies is expected to trigger and fuel SF. However, the ignition of SF depends on the local conditions of the gas. There are several possible reasons why the inflow we detect in GLASS-180009 does not trigger SF.

First, the mass of the gas might be too low to ignite significant SF. According to the empirical relation defined by A. Gallazzi et al. (2014) for local galaxies, a galaxy is nonpassive if its sSFR $\geqslant 0.2/t_U \simeq 8 \times 10^{-11}$ yr^{-1} at the galaxy's redshift. For a stellar mass of $\simeq 4 \times 10^{10}\ M_\odot$, as with GLASS-180009, this implies a $\mathrm{SFR_{min}} \geqslant 3\ M_\odot$ yr^{-1}. Using the scaling relations derived by L. J. Tacconi et al. (2018), we can estimate the expected depletion time of the gas in a galaxy at $z \sim 2.7$ with the stellar mass of GLASS-180009, namely $t_{\rm dep} \simeq 0.5$ Gyr. Then, we can estimate the minimum mass of the gas required to have $\mathrm{SFR_{min}}$ as $M_{\rm gas,min} = \mathrm{SFR_{min}} \times t_{\rm depl} \simeq 2 \times 10^9\ M_\odot$, which is 1 dex larger than the estimated mass of the inflowing neutral gas. Therefore, the reason why GLASS-180009 remains passive could be that the mass of the gas is too low to enhance significant SF. However, this assumes that the total gas mass fueling the SF is that of the inflow, which might not be the case if some gas is also residing in the galaxy.

Another reason why we do not detect a significant SFR might be that the gas density is too low to form stars efficiently. Several works have shown that in nearby galaxies there is a quite sharp transition at $\log(N_{\rm H}) \sim 21$, below which the hydrogen is predominantly neutral, while the molecular H_2 is dominant at higher column densities (L. Blitz & E. Rosolowsky 2006; F. Bigiel et al. 2008; A. K. Leroy et al. 2008; M. R. Krumholz et al. 2009). These works consistently show that the transition in $\log(N_{\rm H})$ corresponds to a gas surface density $\Sigma_{\rm gas} \sim 10\ M_\odot\ \mathrm{pc}^{-2}$, which is exactly the critical threshold found empirically by R. C. Kennicutt (1998) above which SF occurs because the gas becomes gravitationally unstable, according to the theoretical Toomre criterion (see also R. C. Kennicutt 1998; C. L. Martin & R. C. Kennicutt 2001). For GLASS-180009, we estimate $\log(N_{\rm H}/\mathrm{cm}^2) \simeq 20.7$, suggesting that the density could be too low to efficiently convert gas into stars. However, considering the uncertainties on $\log(N_{\rm H})$ discussed in Section 4.3, observations of the H I and H_2 are needed to further probe this argument.

On the other hand, we point out that the works mentioned above discussing the density thresholds are based on galaxies whose gas is already settled. For an inflowing gas, we might instead expect it to compress and ignite the SF as it falls into the galaxy due to compressive turbulence, shocks, or converging flows, on characteristic timescales of the order of 10–100 Myr, depending on the conditions of the gas (D. Hollenbach & E. E. Salpeter 1971; M. Jura 1975; E. A. Bergin et al. 2004; S. C. O. Glover & M.-M. Mac Low 2007). Assuming a constant inflow mass and rate of neutral gas for GLASS-180009, we can estimate the overall timescale for the inflowing gas as $t_{\rm in} \equiv M_{\rm in}/\dot{M}_{\rm in} \simeq 16$ Myr. This is consistent but relatively short compared to the timescales at which the infalling gas is expected to compress the gas and form stars. Therefore, the SFR could be low because the timescale of the infall is too short to compress the gas and ignite SF.

We note that if the inflow is fueling some low-level SF, this is clear direct evidence that galaxies can accrete cold gas and keep forming stars long after their quenching, while remaining quiescent according to the standard diagnostics (e.g., S. Belli et al. 2017, 2021; R. Gobat et al. 2020; N. Salvador-Rusiñol et al. 2020; P. Zhu et al. 2025). If the gas accretion and SF are sustained for several Gyr through continuous or episodic events, the younger populations formed would account for a nonnegligible fraction of the total stellar mass we measure at lower redshifts, as inferred from their SFHs (e.g., S. Tacchella et al. 2022; D. Bevacqua et al. 2024). Alternatively, if no SF is ignited at all, the accreted gas might end up replenishing the neutral gas content of the galaxy, in line with the large dust content found in high-redshift quiescent galaxies (e.g., G. Lorenzon et al. 2025; J. C. Siegel et al. 2025).

Finally, it is possible that the neutral gas is fueling the AGN, assuming a central accretion of the gas. In fact, a link of the neutral gas inflow with the AGN activity in passive galaxies has already been reported in the literature (T. Sato et al. 2009; N. Roy et al. 2021). However, the AGN emissions reported in these works are much stronger, and the accretion rates much lower ($\sim$0.1–5 $M_\odot$ yr^{-1}). Even assuming a very low efficiency, $\eta = 0.01$, the luminosity of the AGN expected from the inflow rate we measure would be $L_{\rm AGN} = \eta\, \dot{M}_{\rm in}\, c^2 \sim 10^{46}$ erg s^{-1}, where c is the speed of light. Assuming $L_{\rm AGN} = 100 \times L_{\rm H\alpha}$ (T. M. Heckman et al. 2004; J. E. Greene & L. C. Ho 2005), we would then expect $L_{\rm H\alpha} \sim 10^{44}$ erg s^{-1}, which is almost 5 dex higher than the observed luminosity (Section 4.2). Conversely, for the measured $L_{\rm H\alpha} \sim 2 \times 10^{39}$ erg s^{-1}, we would expect $L_{\rm AGN} \sim 2 \times 10^{41}$ erg s^{-1}, implying $\dot{M}_{\rm in} \sim 3 \times 10^{-4}\ M_\odot$ yr^{-1} (assuming $\eta = 0.01$), i.e., about 5 dex lower than the estimated inflowing mass. Thus, it seems unlikely that the infalling gas is powering the AGN. However, the intrinsic flux of the emission lines could be significantly underestimated due to orientation effects. Furthermore, the inflowing material could accumulate in the accretion disk of the AGN rather than falling directly onto the black hole, so that the inflowing gas and the accretion rate might not be directly correlated. Therefore, with current data, we cannot rule out the AGN. Spatially resolved observations of the gas are needed to further probe this possibility.

6. Conclusions

We have reported the spectroscopic detection of neutral gas inflow in a massive quiescent galaxy, GLASS-180009, with $M_* \simeq 4 \times 10^{10}\ M_\odot$ observed at $z_{\rm spec} = 2.6576$ with JWST. From the absorption features of Na I at $\lambda\lambda$5890, 5896, we have derived the mass, $1.6^{+0.1}_{-0.1} \times 10^8\ M_\odot$, and rate, $19^{+6}_{-7}\ M_\odot$ yr^{-1}, of the inflowing neutral gas.

With current observations, we cannot determine the source of the neutral gas. By examining its environment, we found that GLASS-180009, which resides in an overdensity, is surrounded by several galaxies within a projected radius of 150 kpc at comparable redshifts, making them potential source candidates of the inflowing material. Other viable sources of the inflow are the IGM and cosmic filaments, while a galactic fountain seems unlikely.

An inflow of neutral gas is usually associated with enhanced SF. However, we estimated an upper limit to the $\mathrm{SFR} \leqslant 0.2\ M_\odot$ yr^{-1} and $\mathrm{sSFR} \leqslant 0.5 \times 10^{-11}$ yr^{-1}, implying that GLASS-180009 is quiescent. Furthermore, according to its SFH, the galaxy has remained passive during the past $\sim$1 Gyr. On the basis of the estimated properties, we conclude that the inflowing gas is likely not massive or dense enough, or that the duration of the inflow is too short to enhance significant SF. Finally, it is also possible that the inflowing material is accreted at the center of the galaxy, fueling the AGN rather than the SF, although no strong AGN lines are detected.

The detection of neutral gas inflow in a passive galaxy offers a unique view of the postquenching phase of quiescent galaxies at high redshifts. This system could prove that quiescent galaxies can accrete material without necessarily

triggering SF or AGN activity long after their quenching. The fact that this galaxy resides in an overdensity makes this case even more interesting. Understanding the origin and fate of the inflowing gas would provide an unique insight into the complexity of the gas cycle of galaxies in dense environments, which is crucial for models of galaxy evolution. To this end, targeted, deeper multiwavelength observations of this galaxy are necessary. Observations with the integral field unit of JWST would allow us to recover the spatial distribution and resolved kinematics of the inflowing gas and trace its origin. Observations with higher S/N would allow us to further constrain the properties of the gas using other features, such as Mg II and Fe I. ALMA observations targeting neutral and molecular hydrogen would provide more robust constraints on the properties of the inflowing gas.

Acknowledgments

The authors acknowledge financial support from programs HST-GO-17231 and HST-GO-17226, provided through a grant from the STScI under NASA contract NAS5-26555, and program JWST-GO-02561, provided through a grant from the STScI under NASA contract NAS5-03127. F.L.B. acknowledges support from the INAF Mini-Grant 1.05.23.04.01. S.B. is supported by ERC grant 101076080. P.J.W. acknowledges support from the INAF Large Grant 2022 "Extragalactic Surveys with JWST" (PI: Pentericci). P.J.W. is supported by the European Union – NextGenerationEU RFF M4C2 1.1 PRIN 2022 project 2022ZSL4BL INSIGHT. P.J.W. acknowledges support from the INAF Mini-Grant "1.05.24.07.01 RSN 1: Spatially Resolved Near-IR Emission of Intermediate-Redshift Jellyfish Galaxies" (PI: Watson). X.W. is supported by the China Manned Space Program with grant No. CMS-CSST-2025-A06, National Natural Science Foundation of China (grant No. 12373009), the CAS Project for Young Scientists in Basic Research (grant No. YSBR-062), and Fundamental Research Funds for the Central Universities, the Xiaomi Young Talents Program.

The JWST data presented in this article are available from the DJA (https://dawn-cph.github.io/dja/index.html) and from the Mikulski Archive for Space Telescopes (MAST) at the STScI (doi:10.17909/wef3-rf26).

Software: `NumPy` (C. R. Harris et al. 2020); `SciPy` (P. Virtanen et al. 2020); `Astropy` (Astropy Collaboration et al. 2022); `matplotlib` (J. D. Hunter 2007); `pPXF` (M. Cappellari 2023); `VoigtFit` (J.-K. Krogager 2018); `emcee` (D. Foreman-Mackey et al. 2013) `BAGPIPES` (A. C. Carnall et al. 2018); `Pathfinder` (K. G. Iyer et al. 2024).

Appendix A
Wavelength Calibration and Photometric Rescaling

Concerning the reliability of the JWST spectra, D. Bevacqua et al. (2025) showed that they may be affected by calibration issues (see also F. D'Eugenio et al. 2025). Specifically, the authors pointed out a mismatch between the fluxes of the PRISM and grating spectra that increases with wavelength. For this reason, we checked the reliability of the wavelength calibration by comparing the fluxes of the PRISM and the grating spectra (degraded to the resolution of the PRISM), as shown in the lower panels of Figure 6. We found that the flux of the grating spectra is about 15% lower than that of the prism. However, we did not find evidence for a dependence on wavelength, implying no evident calibration issues.

We also compared the flux of the grating spectra with that of the photometric data. To this aim, we integrated the flux of the spectra over the NIRCam filters, weighted it with the transmission functions, and compared it with the NIRCam photometry. We found that the photometric fluxes are, on average, ∼50% higher than those of the spectra, with a variation of about ±20% (consistent with the uncertainties of the spectrum and photometry combined), but without any significant dependence on the wavelength. Therefore, we rescaled the flux of the high-resolution spectrum to the photometry, using a polynomial of degree 8.

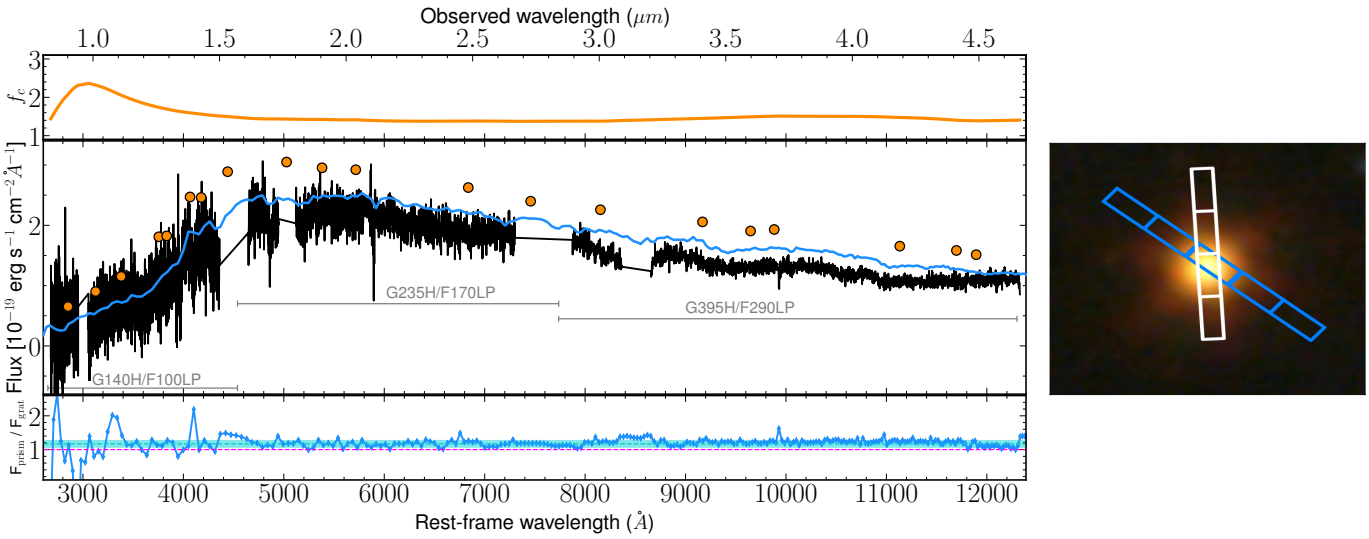

Figure 6. Left panel: spectroscopic and photometric data of GLASS-180009. In the central panel, we show original (i.e., not scaled to the photometry) grating (black curve) and PRISM (blue curve) spectra; the orange circles are the photometric data. In the upper panel, we show the correction factor, f_c, applied over the grating spectrum to rescale it to the photometric data. We estimate a median value $f_c = 1.5$, with no evident dependence on the wavelength. In the lower panel, we show the flux ratio between the PRISM spectrum and the high-resolution spectrum with blue diamonds. The dashed blue lines and shaded region indicate the median and 1σ error of the ratio. The dashed magenta horizontal line marks the 1-to-1 ratio. The flux ratio shows that there is no evident issue with the wavelength calibration. Right panel: F444W image of the galaxy. The footprints of the NIRSpec microshutters for the gratings and PRISM are overplotted in white and blue, respectively.

Appendix B
Estimates of Effective Radius and Sérsic Index

To estimate the effective radius and Sérsic index, we use `pysersic` (I. Pasha & T. B. Miller 2023), a Bayesian inference fitting tool, to fit the F277W image from UNCOVER with a 1D Sérsic profile. Background sources were masked using the UNCOVER Data Release 3 segmentation map. We sample the marginalized posteriors using a no U-turn sampler using two chains with 750 warm-up and 500 sampling steps each (M. D. Hoffman & A. Gelman 2014). We show the best-fit `pysersic` image in Figure 7. As a result, we found a best-fit $R_e = 1.05^{+0.01}_{-0.01}$ kpc and $n = 2.15^{+0.01}_{-0.01}$.

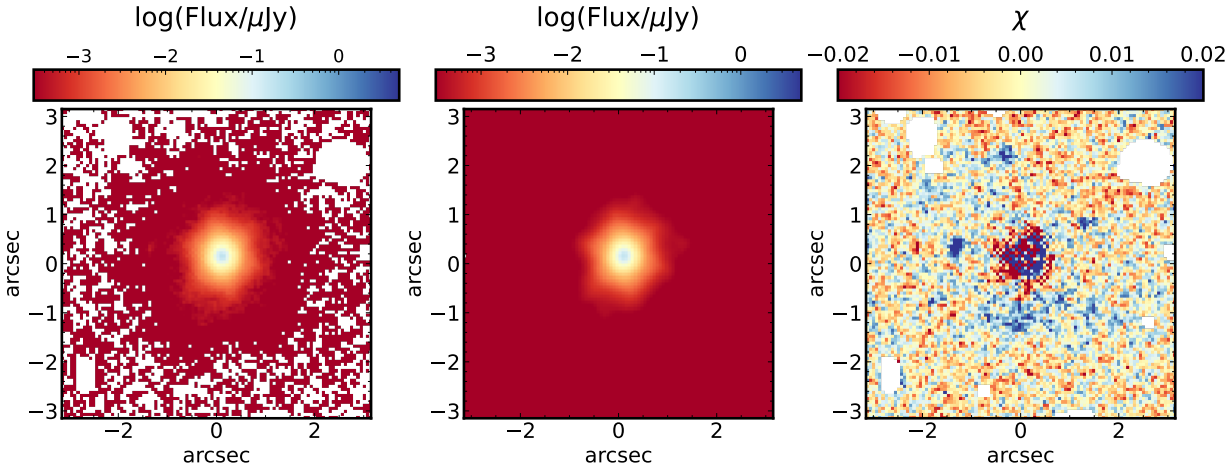

Figure 7. Fit of the F277W image with `pysersic`. The left and central panels are the observed and best-fit model images, while the right panel shows the χ map, i.e., the residuals divided by the errors.

Appendix C
Testing the Fits of the Stellar Population Properties

In this section, we test the reliability of the derived stellar population properties. In particular, we want to probe whether including very young models affects the results. Toward this aim, we considered the stellar population models of G. Bruzual & S. Charlot (2003), updated to version 2016 (hereafter BC16). Following the same methods described in Section 3.2, we fit the high-resolution JWST spectrum with `pPXF`, adopting the BC16 models and including ages as young as 1 Myr. However, in this case, we limit the fit to the rest-frame $\lambda < 1\mu$m, as the BC16 models have a lower resolution than the JWST spectrum at longer wavelengths. From this fit, we estimate a mass-weighted age of 1.4 Gyr and a supersolar metallicity of [M/H] = 0.3 dex, approximately 0.4 Gyr lower and 0.6 dex higher than the values estimated with the EMILES models. However, as evident from the SFH shown in Figure 8, we find that the best-fitting spectrum contains no contribution from young stellar components. Moreover, we estimate the same quenching time $t_{95} \simeq 1$ Gyr as with the EMILES models. We verified that the difference in the results is due to both the different wavelength range fit and intrinsic differences in the adopted models (isochrones, stellar libraries, etc.).

As a further independent check, we fit the high-resolution spectrum with `Bagpipes` (A. C. Carnall et al. 2018), adopting the same assumptions as for the fits with `pPXF` (Section 3.2) and using the BC16 models. The only significant differences are that we parameterize the SFH with a double power-law, we fit the emission lines with a nebular component, and we fit a white-noise scaling factor. A summary of the input parameters is given in Table 3.

We show the SFH derived with `Bagpipes` in Figure 9. The relevant stellar population properties are reported in Table 4. The complete posterior distribution is shown in Figure 10. In general, we find results consistent with the `pPXF` fits when fed with the BC16 models.

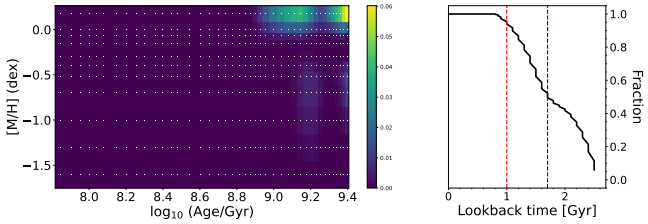

Figure 8. Star formation history derived with `pPXF`, as in Figure 2, but using the BC16 models.

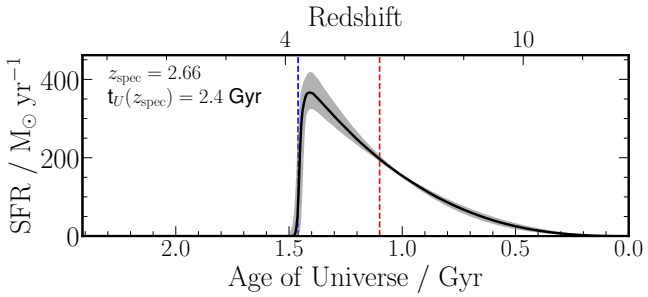

Figure 9. Star formation history derived with `Bagpipes` using the BC16 models. The red and blue lines indicate t_{50} and t_{90}, respectively.

We then conclude that the stellar age and metallicity depend on the adopted models, as well as on the wavelength range fitted (see also D. Bevacqua et al. 2025). However, investigating these differences is beyond the scope of this article. The main results of this section are that including very young models does not change the results. and that all fits consistently indicate that the galaxy quenched ∼1 Gyr before the observations without experiencing any other significant SF event afterwards.

Table 3
`Bagpipes` Input Parameters

Component	Parameter	Symbol/Unit	Range	Prior
General	Redshift	z	(2.5, 2.8)	Uniform
	Stellar velocity dispersion	σ_*/km s^{-1}	(50, 500)	Logarithmic
SFH	Total stellar mass formed	$M_{*,\mathrm{tot}}/M_\odot$	(1, 10^{13})	Logarithmic
	Double power-law falling slope	α	(0.1, 1000)	Logarithmic
	Double power-law rising slope	β	(0.1, 1000)	Logarithmic
	Double power-law turnover time	τ_{dpl}	(0.1, 2.5)	Uniform
Dust	V-band attenuation	A_V/mag	(0, 4)	Uniform
Nebular	Ionization parameter	U	(10^{-4}, 10^{-2})	Logarithmic
	Gas metallicity	$Z_g/Z_\odot$	(0.00355, 3.55)	Logarithmic
Noise	White-noise scaling	s	(0.1, 10)	Logarithmic

Note. For the dust, we assume a D. Calzetti et al. (2000) attenuation law.

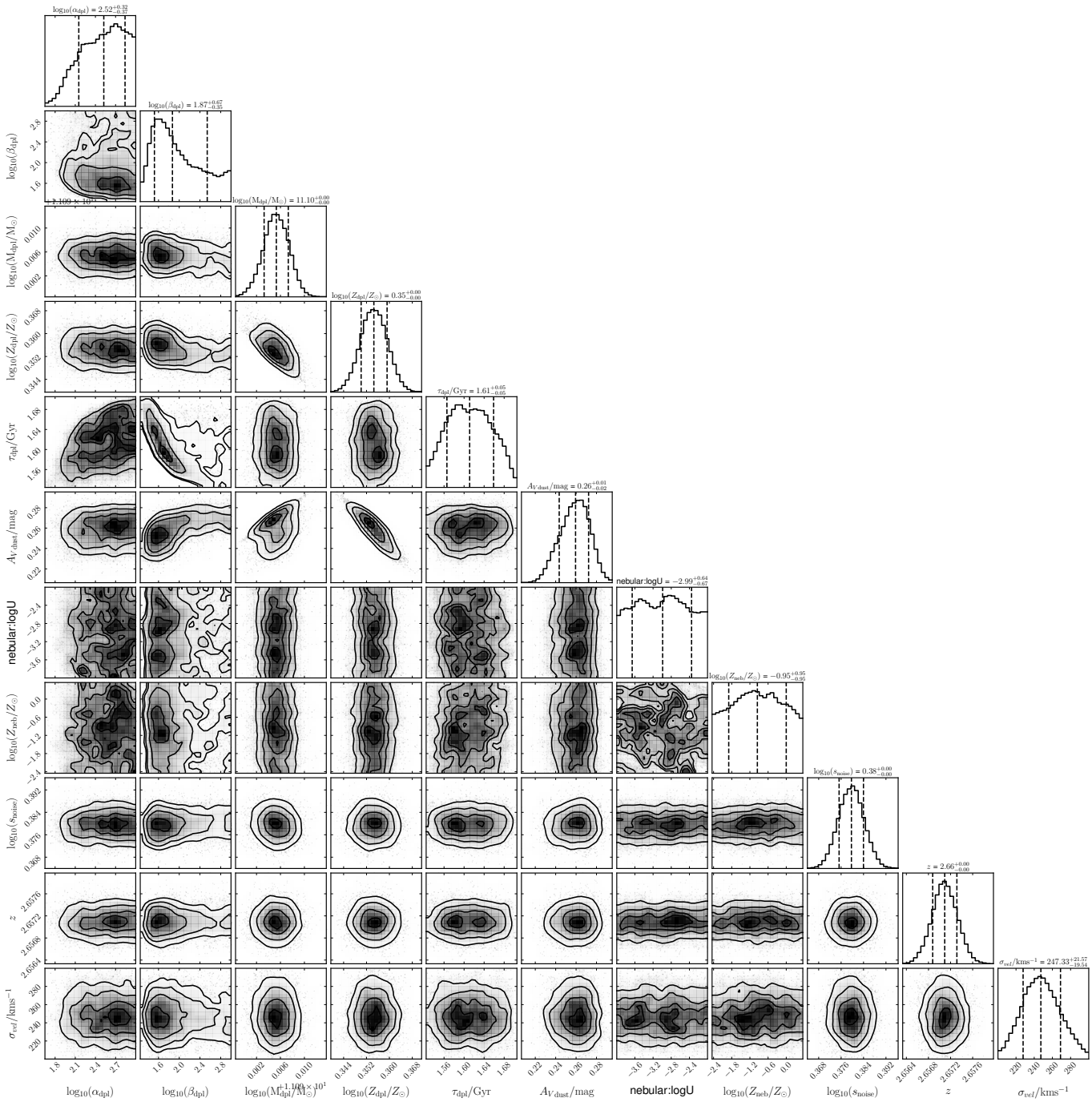

Figure 10. Full posterior distributions of the fitted parameters reported in Table 3. Note that no correction is here applied for the magnification (D. Marchesini et al. 2023).

Table 4
Relevant Stellar Population Parameters Derived with `Bagpipes`

Parameter	Value
$\log_{10}(M_*^{\rm corr}/M_\odot)$	$10.66^{+0.02}_{-0.02}$
$\sigma_*/{\rm km\ s^{-1}}$	247^{+22}_{-20}
$A_V/{\rm mag}$	$0.26^{+0.01}_{-0.02}$
${\rm Age/Gyr}$	$1.32^{+0.06}_{-0.11}$
$\log_{10}(Z_*/Z_\odot)/{\rm dex}$	$0.35^{+0.01}_{-0.01}$
${\rm SFR}/M_\odot\ {\rm yr^{-1}}$	$0.00^{+0.00}_{-0.00}$
$t_{50}/{\rm Gyr}$	$1.40^{+0.08}_{-0.12}$
$t_{95}/{\rm Gyr}$	$0.94^{+0.04}_{-0.03}$

Note. $M_*^{\rm corr}$ is the mass of living stars, corrected for the magnification factor (see D. Marchesini et al. 2023).

Appendix D
Estimate of the [Mg/Fe] Abundance

We estimate the [Mg/Fe] abundance of GLASS-180009 by fitting the spectral indices Mgb and Fe5270. The Mgb index is considered a tracer of Mg abundance, while Fe5270 is considered a tracer of iron abundance (see, e.g., D. Thomas et al. 2003). Other reliable tracers of the iron abundance are Fe4383 and Fe5335. However, the former falls into the detector gap of the NIRSpec spectra, and the latter is significantly affected by bad pixels, so we decided not to use them.

We estimate [Mg/Fe] with the Bayesian full-index fitting (FIF) method described in I. Martín-Navarro et al. (2019, 2021). The FIF method performs a pixel-by-pixel fit of all the spectral pixels within the bandpasses of the fitted spectral features. Here, we adopt `emcee` to maximize the following likelihood function:

$$\ln(\boldsymbol{O}|\boldsymbol{S}) = -\frac{1}{2}\sum_n \left[\frac{(O_n - M_n)^2}{\sigma_n^2} - \ln\left(\frac{1}{\sigma_n^2}\right)\right], \quad \text{(D1)}$$

where the sum extends over all the spectral pixels within the bandpasses fitted, with O_n and M_n being the observed and the model fluxes, respectively, of the nth spectral pixel, while σ_n is the uncertainty on O_n. We perform the fit by keeping the age fixed[24] to the light-weighted best-fitting age of `pPXF`, 1.65 Gyr, while varying the metallicity and [α/Fe]. As for the templates, we adopted the semi-empirical MILES (sMILES) models with variable α-enhancement (A. T. Knowles et al. 2023).

From this fit, we estimate $[\mathrm{M/H}] = -0.36^{+0.20}_{-0.14}$ dex (consistent with the full spectral fitting) and $[\mathrm{Mg/Fe}] = 0.11^{+0.15}_{-0.13}$ dex. We show the posterior distributions and the best fits in Figure 11. We mention that varying the age within the errors provides consistent results. Overall, the quality of the spectrum is not sufficient to robustly constrain the [Mg/Fe], but our fits indicate a moderate α-enhancement, comparable to quiescent galaxies at lower redshifts (e.g., D. Bevacqua et al. 2023).

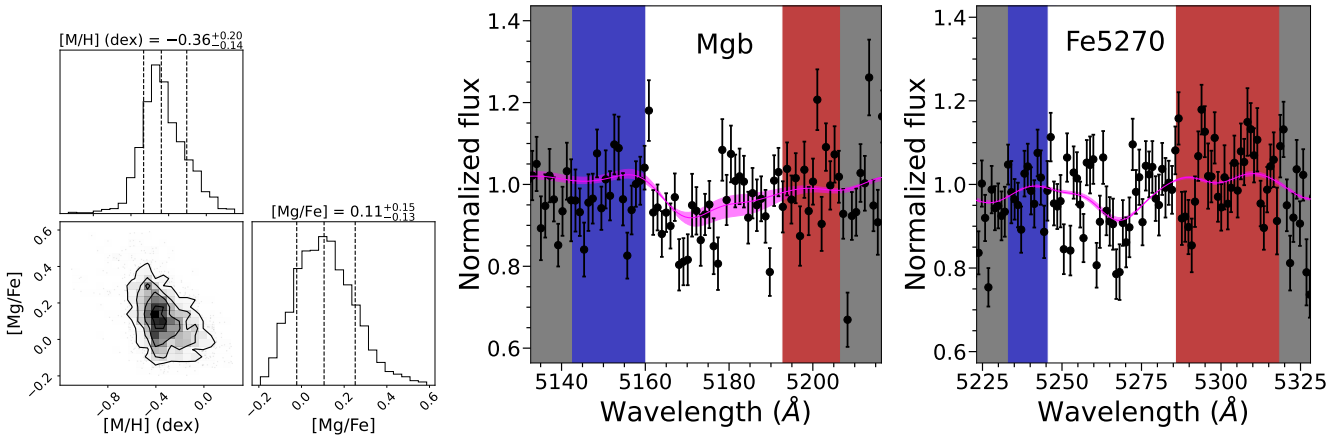

Figure 11. Best-fitting solution for the [Mg/Fe] abundance with the FIF method. In the left panel, we show a corner plot of the posterior distributions. In the central and right panels, we show the observed spectral indices (black circles) compared to the best-fit models (magenta line). The blue and red vertical regions indicate the wavelength regions of the blue and red pseudo-continua, respectively, while the white central region is the feature.

[24] This is because the robust spectral indices sensitive to the age are the Balmer lines, which are however affected by line emissions.

Appendix E
ALMA-DUALZ Observations

In Figure 12, we show ALMA imaging from DUALZ (S. Fujimoto et al. 2025). The image shows the same sky region as shown in Figure 5 in the 244–274 GHz frequency band, corresponding to rest-frame $\lambda \sim 0.3$ mm. The image is dominated by noise and does not show any clear detection of gas around GLASS-180009 or the surrounding galaxies. Therefore, from these observations, we cannot probe the origin and distribution of the neutral gas.

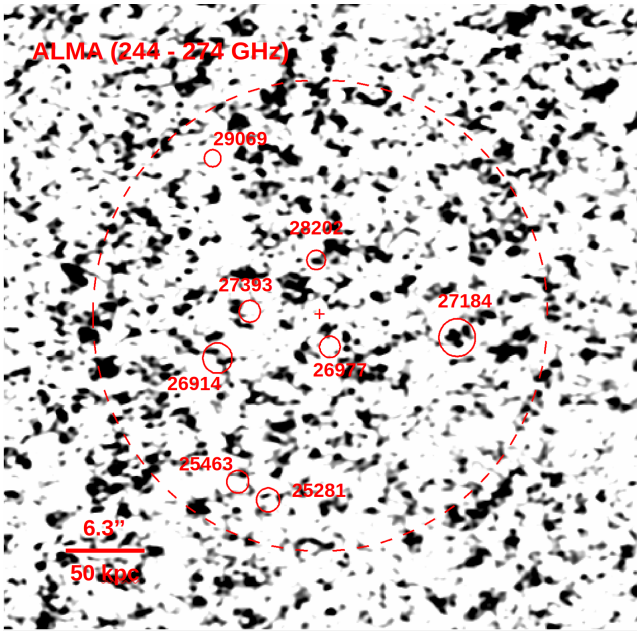

Figure 12. ALMA observations of the same sky region as in Figure 5; the symbols are the same.

ORCID iDs

Davide Bevacqua https://orcid.org/0000-0001-8863-2472
Danilo Marchesini https://orcid.org/0000-0001-9002-3502
Richard Pan https://orcid.org/0000-0002-9651-5716
Sirio Belli https://orcid.org/0000-0002-5615-6018
Gabriel Brammer https://orcid.org/0000-0003-2680-005X
Guido De Marchi https://orcid.org/0000-0001-7906-3829
Giovanna Giardino https://orcid.org/0000-0002-9262-7155
Karl Glazebrook https://orcid.org/0000-0002-3254-9044
Valentina La Torre https://orcid.org/0009-0002-5758-6025
Jamie Lin https://orcid.org/0000-0002-3101-8348
Adam Muzzin https://orcid.org/0000-0002-9330-9108
Namrata Roy https://orcid.org/0000-0002-4430-8846
Paola Santini https://orcid.org/0000-0002-9334-8705
Benedetta Vulcani https://orcid.org/0000-0003-0980-1499
Peter J. Watson https://orcid.org/0000-0003-3108-0624
Xin Wang https://orcid.org/0000-0002-9373-3865

References

Astropy Collaboration, Price-Whelan, A. M., Lim, P. L., et al. 2022, ApJ, 935, 167
Baldwin, J. A., Phillips, M. M., & Terlevich, R. 1981, PASP, 93, 5
Balogh, M. L., Morris, S. L., Yee, H. K. C., Carlberg, R. G., & Ellingson, E. 1999, ApJ, 527, 54
Beifiori, A., Thomas, D., Maraston, C., et al. 2014, ApJ, 789, 92
Belfiore, F., Maiolino, R., Maraston, C., et al. 2016, MNRAS, 461, 3111
Belli, S., Genzel, R., Förster Schreiber, N. M., et al. 2017, ApJL, 841, L6
Belli, S., Contursi, A., Genzel, R., et al. 2021, ApJL, 909, L11
Ben Bekhti, N., Richter, P., Westmeier, T., & Murphy, M. T. 2008, A&A, 487, 583
Bergin, E. A., Hartmann, L. W., Raymond, J. C., & Ballesteros-Paredes, J. 2004, ApJ, 612, 921
Bernardi, M., Sheth, R. K., Domínguez Sánchez, H., et al. 2023, MNRAS, 518, 3494
Bevacqua, D., Saracco, P., Boecker, A., et al. 2024, A&A, 690, A150
Bevacqua, D., Saracco, P., La Barbera, F., et al. 2023, MNRAS, 525, 4219
Bevacqua, D., Saracco, P., La Barbera, F., et al. 2025, A&A, 699, A203
Bezanson, R., Labbe, I., Whitaker, K. E., et al. 2024, ApJ, 974, 92
Bigiel, F., Leroy, A., Walter, F., et al. 2008, AJ, 136, 2846
Blitz, L., & Rosolowsky, E. 2006, ApJ, 650, 933
Brammer, G. 2022, msaexp: NIRSpec Analyis Tools 0.3, Zenodo, doi:10.5281/zenodo.7299500
Bruzual, G., & Charlot, S. 2003, MNRAS, 344, 1000
Calzetti, D., Armus, L., Bohlin, R. C., et al. 2000, ApJ, 533, 682
Cappellari, M. 2017, MNRAS, 466, 798
Cappellari, M. 2023, MNRAS, 526, 3273
Cappellari, M., Bacon, R., Bureau, M., et al. 2006, MNRAS, 366, 1126
Cappellari, M., McDermid, R. M., Alatalo, K., et al. 2012, Natur, 484, 485
Carnall, A. C., McLure, R. J., Dunlop, J. S., & Davé, R. 2018, MNRAS, 480, 4379
Carnall, A. C., Cullen, F., McLure, R. J., et al. 2024, MNRAS, 534, 325
Chabrier, G. 2003, PASP, 115, 763
Chauke, P., van der Wel, A., Pacifici, C., et al. 2019, ApJ, 877, 48
Cid Fernandes, R., Stasińska, G., Mateus, A., & Vale Asari, N. 2011, MNRAS, 413, 1687
Coleman, E., G.C., K. V., Chen, Y., et al. 2024, ApJL, 977, L23
Conroy, C., Dutton, A. A., Graves, G. J., Mendel, J. T., & van Dokkum, P. G. 2013, ApJL, 776, L26
Conroy, C., Villaume, A., van Dokkum, P. G., & Lind, K. 2018, ApJ, 854, 139
Davé, R., Crain, R. A., Stevens, A. R. H., et al. 2020, MNRAS, 497, 146
Davies, R. L., Belli, S., Park, M., et al. 2024, MNRAS, 528, 4976
de Graaff, A., Setton, D. J., Brammer, G., et al. 2025, NatAs, 9, 280
Dekel, A., Sari, R., & Ceverino, D. 2009, ApJ, 703, 785
D'Eugenio, F., Cameron, A. J., Scholtz, J., et al. 2025, ApJS, 277, 4
Dopita, M. A., & Sutherland, R. S. 1995, ApJ, 455, 468
Foreman-Mackey, D., Hogg, D. W., Lang, D., & Goodman, J. 2013, PASP, 125, 306
Fox, A., & Davé, R. 2017, ASSL, 430, 1
Fox, A. J., Richter, P., Ashley, T., et al. 2019, ApJ, 884, 53
French, K. D., Yang, Y., Zabludoff, A. I., & Tremonti, C. A. 2018, ApJ, 862, 2
Fujimoto, S., Bezanson, R., Labbe, I., et al. 2025, ApJS, 278, 45
Furtak, L. J., Zitrin, A., Weaver, J. R., et al. 2023, MNRAS, 523, 4568
Gallazzi, A., Bell, E. F., Zibetti, S., Brinchmann, J., & Kelson, D. D. 2014, ApJ, 788, 72
Glazebrook, K., Nanayakkara, T., Schreiber, C., et al. 2024, Natur, 628, 277
Glover, S. C. O., & Mac Low, M.-M. 2007, ApJ, 659, 1317
Gobat, R., Magdis, G., D'Eugenio, C., & Valentino, F. 2020, A&A, 644, L7
Grand, R. J. J., van de Voort, F., Zjupa, J., et al. 2019, MNRAS, 490, 4786
Greene, J. E., & Ho, L. C. 2005, ApJ, 630, 122
Harris, C. R., Millman, K. J., van der Walt, S. J., et al. 2020, Natur, 585, 357
Heckman, T. M., Kauffmann, G., Brinchmann, J., et al. 2004, ApJ, 613, 109
Ho, S. H., Martin, C. L., Kacprzak, G. G., & Churchill, C. W. 2017, ApJ, 835, 267
Hoffman, M. D., & Gelman, A. 2014, JMLR, 15, 1593
Hollenbach, D., & Salpeter, E. E. 1971, ApJ, 163, 155
Hunter, J. D. 2007, CSE, 9, 90
Iyer, K. G., Yunus, M., O'Neill, C., et al. 2024, ApJS, 275, 38
Jorgensen, I., Franx, M., & Kjaergaard, P. 1995, MNRAS, 276, 1341
Jura, M. 1975, ApJ, 197, 575
Kacprzak, G. G., Churchill, C. W., Steidel, C. C., Spitler, L. R., & Holtzman, J. A. 2012, MNRAS, 427, 3029
Kauffmann, G., Heckman, T. M., White, S. D. M., et al. 2003, MNRAS, 341, 33
Kennicutt, R. C., Jr. 1989, ApJ, 344, 685
Kennicutt, R. C., Jr. 1998, ApJ, 498, 541
Kewley, L. J., Geller, M. J., & Jansen, R. A. 2004, AJ, 127, 2002
Kewley, L. J., Groves, B., Kauffmann, G., & Heckman, T. 2006, MNRAS, 372, 961
Knowles, A. T., Sansom, A. E., Vazdekis, A., & Allende Prieto, C. 2023, MNRAS, 523, 3450

Krogager, J.-K. 2018, arXiv:1803.01187
Krug, H. B., Rupke, D. S. N., & Veilleux, S. 2010, ApJ, 708, 1145
Krumholz, M. R., McKee, C. F., & Tumlinson, J. 2009, ApJ, 693, 216
La Barbera, F., Ferreras, I., Vazdekis, A., et al. 2013, MNRAS, 433, 3017
La Barbera, F., Vazdekis, A., Ferreras, I., et al. 2019, MNRAS, 489, 4090
Leroy, A. K., Walter, F., Brinks, E., et al. 2008, AJ, 136, 2782
Liboni, C., Belli, S., Bugiani, L., et al. 2025, arXiv:2506.05470
Lorenzon, G., Donevski, D., Lisiecki, K., et al. 2025, A&A, 693, A118
Lovell, M. R., Pillepich, A., Genel, S., et al. 2018, MNRAS, 481, 1950
Mancini, C., Daddi, E., Juneau, S., et al. 2019, MNRAS, 489, 1265
Marasco, A., Fraternali, F., & Binney, J. J. 2012, MNRAS, 419, 1107
Marchesini, D., Brammer, G., Morishita, T., et al. 2023, ApJL, 942, L25
Martin, C. L., & Bouché, N. 2009, ApJ, 703, 1394
Martin, C. L., & Kennicutt, R. C., Jr. 2001, ApJ, 555, 301
Martín-Navarro, I., La Barbera, F., Vazdekis, A., Falcón-Barroso, J., & Ferreras, I. 2015, MNRAS, 447, 1033
Martín-Navarro, I., Lyubenova, M., van de Ven, G., et al. 2019, A&A, 626, A124
Martín-Navarro, I., Pinna, F., Coccato, L., et al. 2021, A&A, 654, A59
Mascia, S., Roberts-Borsani, G., Treu, T., et al. 2024, A&A, 690, A2
McConachie, I., Antwi-Danso, J., Chang, W., et al. 2025, arXiv:2508.05752
Mendel, J. T., Beifiori, A., Saglia, R. P., et al. 2020, ApJ, 899, 87
Moretti, L., Belli, S., Rudie, G. C., et al. 2025, arXiv:2507.07160
Murray, N., Martin, C. L., Quataert, E., & Thompson, T. A. 2007, ApJ, 660, 211
Oppenheimer, B. D., & Davé, R. 2008, MNRAS, 387, 577
Pan, R., Suess, K. A., Marchesini, D., et al. 2025, ApJL, 990, L24
Paris, D., Merlin, E., Fontana, A., et al. 2023, ApJ, 952, 20
Pasha, I., & Miller, T. B. 2023, JOSS, 8, 5703
Pietrinferni, A., Cassisi, S., Salaris, M., & Castelli, F. 2004, ApJ, 612, 168
Price, S. H., Bezanson, R., Labbe, I., et al. 2025, ApJ, 982, 51
Putman, M. E. 2017, ASSL, 430, 1
Putman, M. E., Peek, J. E. G., & Joung, M. R. 2012, ARA&A, 50, 491
Remus, R.-S., & Kimmig, L. C. 2025, ApJ, 982, 30
Rey, M. P., Pontzen, A., Agertz, O., et al. 2020, MNRAS, 497, 1508
Richter, P., Krause, F., Fechner, C., Charlton, J. C., & Murphy, M. T. 2011, A&A, 528, A12
Roy, N., Bundy, K., Rubin, K. H. R., et al. 2021, ApJ, 919, 145
Rubin, K. H. R., Juarez, C., Cooksey, K. L., et al. 2022, ApJ, 936, 171
Rubin, K. H. R., Prochaska, J. X., Koo, D. C., & Phillips, A. C. 2012, ApJ, 747, L26
Rubin, K. H. R., Prochaska, J. X., Koo, D. C., et al. 2014, ApJ, 794, 156
Rupke, D. S., & Sanders, D. B. 2005, ApJS, 160, 115
Rupke, D. S. N., Thomas, A. D., & Dopita, M. A. 2021, MNRAS, 503, 4748
Salvador-Rusiñol, N., Vazdekis, A., La Barbera, F., et al. 2020, NatAs, 4, 252
Sánchez-Blázquez, P., Peletier, R. F., Jiménez-Vicente, J., et al. 2006, MNRAS, 371, 703
Sargent, M. T., Daddi, E., Bournaud, F., et al. 2015, ApJL, 806, L20
Sato, T., Martin, C. L., Noeske, K. G., Koo, D. C., & Lotz, J. M. 2009, ApJ, 696, 214
Savage, B. D., & Sembach, K. R. 1996, ApJ, 470, 893
Shipley, H. V., Lange-Vagle, D., Marchesini, D., et al. 2018, ApJS, 235, 14
Siegel, J. C., Setton, D. J., Greene, J. E., et al. 2025, ApJ, 985, 125
Slob, M., Kriek, M., de Graaff, A., et al. 2025, A&A, 702, A110
Spilker, J., Bezanson, R., Barišić, I., et al. 2018, ApJ, 860, 103
Spitoni, E., Matteucci, F., & Marcon-Uchida, M. M. 2013, A&A, 551, A123
Spitoni, E., Matteucci, F., Recchi, S., Cescutti, G., & Pipino, A. 2009, A&A, 504, 87
Stokes, G. M. 1978, ApJS, 36, 115
Suess, K. A., Weaver, J. R., Price, S. H., et al. 2024, ApJ, 976, 101
Tacchella, S., Conroy, C., Faber, S. M., et al. 2022, ApJ, 926, 134
Tacchella, S., Dekel, A., Carollo, C. M., et al. 2016, MNRAS, 457, 2790
Tacchella, S., Forbes, J. C., & Caplar, N. 2020, MNRAS, 497, 698
Tacconi, L. J., Genzel, R., Saintonge, A., et al. 2018, ApJ, 853, 179
Tanaka, T. S., Shimasaku, K., Tacchella, S., et al. 2024, PASJ, 76, 1
Thomas, D., Maraston, C., & Bender, R. 2003, MNRAS, 339, 897
Tortora, C., Napolitano, N. R., Saglia, R. P., et al. 2014, MNRAS, 445, 162
Treu, T., Roberts-Borsani, G., Bradac, M., et al. 2022, ApJ, 935, 110
Valentino, F., Heintz, K. E., Brammer, G., et al. 2025, A&A, 699, A358
van de Sande, J., Kriek, M., Franx, M., et al. 2013, ApJ, 771, 85
van Dokkum, P., Conroy, C., Villaume, A., Brodie, J., & Romanowsky, A. J. 2017, ApJ, 841, 68
van Gorkom, J. H., Knapp, G. R., Ekers, R. D., et al. 1989, AJ, 97, 708
Vazdekis, A., Koleva, M., Ricciardelli, E., Röck, B., & Falcón-Barroso, J. 2016, MNRAS, 463, 3409
Veilleux, S., Maiolino, R., Bolatto, A. D., & Aalto, S. 2020, A&ARv, 28, 2
Virtanen, P., Gommers, R., Oliphant, T. E., et al. 2020, NatMe, 17, 261
Wang, B., Leja, J., Labbé, I., et al. 2024, ApJS, 270, 12
Watson, P. J., Vulcani, B., Treu, T., et al. 2025, A&A, 699, A225
Weaver, J. R., Cutler, S. E., Pan, R., et al. 2024, ApJS, 270, 7
Weldon, A., Reddy, N. A., Topping, M. W., et al. 2023, MNRAS, 523, 5624
White, S. D. M., & Rees, M. J. 1978, MNRAS, 183, 341
Wild, V., Walcher, C. J., Johansson, P. H., et al. 2009, MNRAS, 395, 144
Woodrum, C., Williams, C. C., Rieke, M., et al. 2022, ApJ, 940, 39
Wu, P.-F. 2025, ApJ, 978, 131
Zahid, H. J., & Geller, M. J. 2017, ApJ, 841, 32
Zhu, P., Suess, K. A., Kriek, M., et al. 2025, ApJ, 981, 60
Zolotov, A., Dekel, A., Mandelker, N., et al. 2015, MNRAS, 450, 2327